Aarhus University
Faculty of Science
Department of Physics and Astronomy

PhD Thesis

Dynamical Control of Matter Waves in Optical Lattices

by

Sune Schøtt Mai

November 2010

This thesis has been submitted to the Faculty of Science at Aarhus University in order to fulfill the requirements for obtaining a PhD degree in physics. The work has been carried out under the supervision of professor Klaus Mølmer and associate professor Jan Arlt at the Department of Physics and Astronomy.

Contents

Preface

When I joined Michael Budde's *Quantum Gas Laboratory* at Aarhus University as MSc-student in autumn 2005, the sensation of the rapid development that has taken place in the field of cold quantum gasses over the last decades, was immediately felt. The ^{87}Rb based BEC-experiment had been designed for future addition of an additional atomic species (lithium), it provided coils designed for doing Feshbach physics and had good optical access for multi-axis imaging and 3D optical lattices.

At the time we were working toward observing Bose-Einstein condensation in our own experimental setup. And though this was in itself not much of a novelty in the international physics community already back then, the many ideas of what - hopefully - new and exciting experiments to plan for, made it an extremely inspiring environment to work in. With successful achievement of Bose-Einstein condensation in early 2006 the path was thus open for these experiments. A key feature for these was the addition of 3D optical lattices to the setup, which Henrik Kjær Andersen implemented within his PhD.

At the time of finishing my MSc thesis early 2007, the status and stability of the experimental setup was thus quite good. As an example, I remember giving "live" demonstrations of Bose-Einstein condensation, and even the 3D lattice Mott-insulator transition, to visiting high-school classes. There was no need to be there long time in advance, however, because the system was so stable that BECs could always be produced within 15 minutes after arriving in the lab. This experimental consistency is a testimony of both Michael Budde's design, as well as both Jesper Fevre Bertelsen's and Henrik Kjær Andersen's careful initial buildup of the experiment.

Continuing as PhD student in the lab, my first project was a restructuring of the laboratory computer control system, which could not practically be scaled to include the planned addition of a second atomic species. A "home-designed" FPGA-based solution was settled for, which I started developing. It was also decided to hire a new post-doc to implement the lithium setup, and the experimental plans as a whole seemed well underway.

Shortly before the new post-doc Sung Jong Park's actual arrival, however, Michael Budde announced that he would be leaving the university in favour of a private company. Quite obviously, this new situation was unexpected for everybody, and there was a period of time where it wasn't really clear what would happen, at least not to us left in the group. The message that did come through to Sung Jong and myself was that a new group leader would probably be hired within half a year (i.e. summer 2008), and that we shouldn't make any larger plans or investments in laboratory equipment until then, but simply finish up some smaller lab projects. As time went on, however, the expected date of having a new group leader was continuously postponed, and it became clear to Sung Jong and myself that we had to come up with our own experimental plans.

Sung Jong and I approached the situation a bit differently. He was quite optimistic that publishable results would come out of BEC experiments that would basically be fully analyzable in a non-interacting, mean-field, scalar model, i.e. essentially the single particle Schrödinger equation. While I, being less optimistic in this respect, started discussing the possibilities of doing spin-changing interaction experiments in optical lattices with my official theoretical supervisor Klaus Mølmer, in addition to the lab activities.

Sung Jong's experimental approach proved to be extremely fruitful, yielding large amounts of good and interesting experimental data. Some of this data we could readily interpret, but needed a good angle of approach to actually get it published, while other experiments gave interesting, but at the time not fully understandable results.

With the arrival of the new group leader Jan Arlt and post-doc Jacob Sherson in early summer 2010, suitable perspectives for publication were found on some of our older data. Additionally, some of the previously unexplained observations have triggered a renewed and still ongoing experimental and theoretical investigation. I look forward to getting both our older data published, as well as the very new and exciting results on localized states, which we are now beginning to understand in more detail.

Chapter 1

Introduction

1.1 Thesis Outline

The field of ultra-cold quantum gases has experienced a tremendous evolution since the ground-breaking achievement of Bose-Einstein condensation in 1995 [4, 12]. Today many sub-disciplines exist within the cold quantum gas world, which span a large parameter space: Bosonic or Fermionic particles and their mixtures, atomic or molecular particles, static or controllable interactions and scalar or spinor condensates, just to name some of the keywords that distinguish the many research groups dealing with ultra-cold quantum gases.

In this context, the present thesis is closely tied to the physics of Bose-Einstein condensates in optical lattices. It is structured closely around 3 up-coming publications, and the list of chapters covers the following subjects.

- Chapter 1 is a general introduction to the physics underlying Bose-Einstein condensation.

- Chapter 2 is a brief overview of our experimental setup. Most of this is covered in detail elsewhere, but included here for completeness.

- Chapter 3 is an introduction to the physics of optical lattices used in the articles, i.e. the AC Stark shift and the non-interacting single particle band-structure.

- Chapter 4 presents our experiments on optical lattice calibration techniques.

- Chapter 5 demonstrates time-dependent optical lattice control as a versatile tool with applications to e.g. matter wave interferometry.
- Chapter 6 presents recent results on wave-packet dynamics and localized states, which have turned out to fit very well with the theoretical description used in the time-dependent lattice control chapter.
- As a separate appendix, an introduction is given to an FPGA-based laboratory control system, which I have developed as part of my PhD. This is not connected with the rest of the thesis, but is included as a quick overview chapter for future group members.

1.2 Bose-Einstein Condensation

Bose-Einstein condensation of Bosonic atoms can be derived as a consequence of thermodynamics and Bosonic statistics. The current chapter briefly reviews the basic steps leading to the prediction of the condensation.

If we make the simplifying approximation that the atoms are *non-interacting* (and have no spin), we can write the Hamiltonian, H, as a sum over single particle spatial modes [39, eq. 2.3.8]

$$H = \sum_k \hbar\omega_k \hat{n}_k \tag{1.1}$$

where $\hat{n}_k = a_k^\dagger a_k$.

Following [39, eqs. 3.4.35, 3.4.41] we define the entropy of the system in terms of the density operator as

$$S = -k_B \mathrm{tr}\big(\rho \ln(\rho)\big) \tag{1.2}$$

Using that ρ is diagonal in the single-particle spatial mode occupation number basis, $\bar{n}$, this is

$$S = -k_B \sum_{\bar{n}} \rho_{\bar{n}\bar{n}} \ln(\rho_{\bar{n}\bar{n}}) \tag{1.3}$$

The basic postulate of thermodynamics is that the entropy in equilibrium is maximized, subject to the relevant constraints. In our case, these constraints are the ensemble average of the energy, $U = \mathrm{tr}(\rho H)$, [39, eq. 3.4.44] and the number of atoms, $N = \sum_k n_k$, in addition to the overall normalization of ρ.

We maximize $\sigma = \frac{1}{k_B} S$ subject to this set of constraints using the method of *Lagrange multipliers* [20, 39]. Under a (diagonal) variation $\delta\rho_{\bar{n}\bar{n}}$, the first order variation in σ is

$$\delta\sigma = -\sum_{\bar{n}} \delta\rho_{\bar{n}\bar{n}} \big(\ln(\rho_{\bar{n}\bar{n}}) + 1\big) \tag{1.4}$$

The variation in U is similarly

$$\delta U = \sum_{\bar{n}} \delta\rho_{\bar{n}\bar{n}} \sum_{k=0}^{\infty} \hbar\omega_k n_k \tag{1.5}$$

while the variation in N is

$$\delta N = \sum_{\bar{n}} \delta\rho_{\bar{n}\bar{n}} \sum_{k=0}^{\infty} n_k \tag{1.6}$$

At last, we need to keep the probability-normalization $\mathrm{tr}(\rho) = 1$ fixed. To this end we write the variation

$$\delta\mathrm{tr}(\rho) = \sum_{\bar{n}} \delta\rho_{\bar{n}\bar{n}} \tag{1.7}$$

To carry out the constrained optimization, we introduce the Lagrange multipliers β for the constraint on U, $-\beta\mu$ for the constraint on N (to comply with common notation) and γ for the normalization constraint. An extremum is then given by solutions to

$$\delta\sigma - \beta\delta U + \beta\mu\delta N - \gamma\delta\mathrm{tr}(\rho) = 0 \tag{1.8}$$

Since this must hold for an arbitrary variation $\delta\rho_{\bar{n}\bar{n}}$ it must hold for each term in the sum over $\bar{n}$ separately. Inserting the variations and dividing by $\delta\rho_{\bar{n}\bar{n}}$, we get

$$-\big(\ln(\rho_{\bar{n}\bar{n}}) + 1\big) - \beta \sum_{k=0}^{\infty} \hbar\omega_k n_k + \beta\mu \sum_{k=0}^{\infty} n_k - \gamma = 0 \tag{1.9}$$

The solution for $\rho_{\bar{n}\bar{n}}$ is

$$\rho_{\bar{n}\bar{n}} = \exp\left(-\beta \sum_{k=0}^{\infty} \hbar\omega_k n_k + \beta\mu \sum_{k=0}^{\infty} n_k - \gamma - 1\right) \tag{1.10}$$

Defining the *grand partition function* $\mathcal{Z}$ [28, eq. 11.14]

$$\mathcal{Z} = \sum_{\bar{n}} \exp\left(-\beta \sum_{k=0}^{\infty} \hbar\omega_k n_k + \beta\mu \sum_{k=0}^{\infty} n_k\right) \tag{1.11}$$

we may, instead of adjusting γ to keep ρ is normalized, write (1.10) as

$$\rho_{\bar{n}\bar{n}} = \frac{1}{\mathcal{Z}} \exp\left(-\beta \sum_{k=0}^{\infty} \hbar\omega_k n_k + \beta\mu \sum_{k=0}^{\infty} n_k\right) \tag{1.12}$$

Since both $E = \sum_{k=0}^{\infty} \hbar\omega_k n_k$ and $N = \sum_{k=0}^{\infty} n_k$ are sums over k, we may write $\mathcal{Z}$ and $\rho_{\bar{n}\bar{n}}$ as a products. For $\mathcal{Z}$ this reads

$$\begin{aligned}
\mathcal{Z} &= \sum_{\bar{n}} \prod_{k=0}^{\infty} \exp\left(-\beta\hbar\omega_k n_k + \beta\mu n_k\right) \\
&= \prod_{k=0}^{\infty} \sum_{n_k} \exp\left(-\beta\hbar\omega_k n_k + \beta\mu n_k\right) \\
&= \prod_{k=0}^{\infty} \mathcal{Z}_k
\end{aligned} \tag{1.13}$$

where we've introduced the single state grand partition function $\mathcal{Z}_k$ (see [28, eq. 11.19] for a discussion of the last step).

We can thus write $\rho_{\bar{n}\bar{n}}$ as a product of independent single-state population probabilities

$$\rho_{\bar{n}\bar{n}} = \prod_k \frac{\exp\left(-\beta\hbar\omega_k n_k + \beta\mu n_k\right)}{\mathcal{Z}_k} \tag{1.14}$$

Writing the energies of the single particle states as $\epsilon_k = \hbar\omega_k$, the form of $\mathcal{Z}_k$ is a geometric series [28, eq. 11.21],

$$\mathcal{Z}_k = \sum_{n_k=0}^{\infty} e^{\beta(\mu-\epsilon_k)n_k} \tag{1.15}$$

which converges if and only if $\mu < \epsilon_k$ (since $\beta > 0$). The value is

$$\mathcal{Z}_k = \frac{1}{1 - e^{\beta(\mu-\epsilon_k)}} \tag{1.16}$$

Observe that

$$\frac{\partial \ln(\mathcal{Z}_k)}{\partial\mu} = \frac{1}{\mathcal{Z}_k} \sum_{n_k=0}^{\infty} \beta n_k e^{\beta(\mu-\epsilon_k)n_k} \tag{1.17}$$

Using that the single state population probability is $p_k(n) = \frac{e^{\beta(\mu-\epsilon_k)n}}{Z_k}$, the mean occupation number, $\langle n_k\rangle$, for the single particle state k can thus be expressed as

$$\langle n_k\rangle = \frac{1}{\beta}\frac{\partial \ln(\mathcal{Z}_k)}{\partial\mu} \tag{1.18}$$

Inserting (1.16) and carrying out the differentiation, we finally get

$$\langle n_k \rangle = \frac{1}{e^{\beta(\epsilon_k - \mu)} - 1} \tag{1.19}$$

This is the *Bose-Einstein* distribution. The Lagrange multiplier β is related to the temperature as $\beta = \frac{1}{k_B T}$ (this is the *definition* of temperature), while μ is called the *chemical potential*.

From the Bose-Einstein distribution, the prediction of Bose-Einstein condensation follows trivially. The total (average) number of particles, N, can be written

$$N = \sum_k \langle n_k \rangle \tag{1.20}$$

For most energies, the energy levels are very closely spaced, and we may approximate the sum over single particle states by an integral.

The only exception to the integral approximation arises from the possibility that for the lowest energy state ϵ_0, we have $\epsilon_0 \approx \mu$. In this case (1.19) is seen to be divergent, which implies that the ground-state can have a macroscopic population. This is Bose-Einstein condensation.

In order to estimate at what temperature this might happen, we set $\epsilon_0 = \mu$ and express the *excited* state population as an integral over energies. For a harmonic trap in 3 dimensions with trap frequencies $\omega_x, \omega_y, \omega_z$, the density of states is [38, eq. 2.10]

$$g(\epsilon) = \frac{\epsilon^2}{2\hbar^3 \omega_x \omega_y \omega_z} \tag{1.21}$$

Choosing the zero level for the energy scale to be at ϵ_0, and setting $N = N_{excited}$ to estimate the transition temperature, the integral is then [38, eq. 2.16].

$$N = \int_0^\infty g(\epsilon) \frac{1}{e^{\beta_c \epsilon} - 1} d\epsilon \tag{1.22}$$

where $\beta_c = \frac{1}{k_B T_c}$ and T_c denotes the *critical temperature*.

Carrying out the integration, T_c is given by [38, eq. 2.20]

$$kT_c = \frac{\hbar \bar{\omega} N^{1/3}}{\zeta(3)^{1/3}} \approx 0.94 \hbar \bar{\omega} N^{1/3} \tag{1.23}$$

where $\zeta(x)$ is the Riemann zeta function and $\bar{\omega} = (\omega_x \omega_y \omega_z)^{1/3}$ is the geometric mean of the trap frequencies.

In this chapter we have thus shown that a cloud of non-interacting trapped Bosonic atoms in a harmonic potential will undergo Bose-Einstein condensation at sufficiently low temperatures. This macroscopically occupied quantum-state is a quite extraordinary physical phenomenon as it displays the quantum characteristics known from single atoms and elementary particles on a macroscopic and easily observable scale.

In the laboratory, we can thus take pictures of quantum mechanical wave-phenomena, that before the realization of Bose-Einstein condensation were well known, but could not be manipulated or probed experimentally to the extent that is now possible.

Chapter 2

Experimental Setup and Methods

2.1 Overview

The creation of a BEC involves multiple steps, each of which is an interesting subject in its own right. In our experimental setup (see Fig. 2.1), we largely follow the approach of [25], and more detailed accounts of our implementation can be found in [2, 5, 6]. For completeness and to document recent changes, however, this chapter briefly reviews both the experimental setup and the methods used to obtain a Bose-Einstein Condensate (BEC).

The vacuum chamber consists of two parts separated by a differential pumping hole: A "high pressure" part ($P \sim 2 \times 10^{-10}$ torr) with a cylindrical glass cell, where we cool and trap ^{87}Rb atoms in a Magneto-Optic Trap (MOT). And a "low pressure part" ($P < 10^{-11}$ torr), where the lifetime due to rest gas collisions is about 2 min. A sketch of the vacuum chamber and associated fixed and movable quadrupole-coils is shown in Fig. 2.2.

After the initial accumulation of ^{87}Rb atoms in the MOT, the experimental sequence leading to the creation and detection of a BEC consists of magnetic transport into the low pressure part, forced radio-frequency evaporative cooling in the science chamber and, finally, absorption imaging. These steps are described individually in the following sections.

2.2 Magneto-Optic Trap and Optical Pumping

The MOT setup consists of a cylindrical glass cell with an attached ion-pump and electrically heatable rubidium dispensers. To produce the cooling and re-

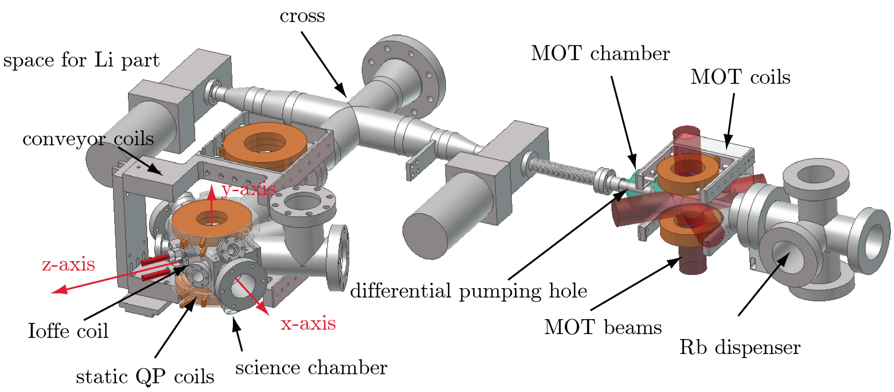

Figure 2.1: CAD drawing of the essential parts of our experimental setup. Ion-pums, titanium sublimation pumps and windows have been removed in the drawing.

pumping light for the MOT, we use a standard diode laser setup [25, 26, 47] placed on a separate laser table. The light is fiber-coupled into 3 polarization maintaining fibers, and close to the MOT each fiber is split using polarizing maintaining 50/50 fiber beam-splitters. This provides balanced intensity levels for the 3 pairs of counter-propagating MOT laser beams, even in case of drifting fiber-coupling efficiencies. Six telescopes with built-in $\lambda/4$-plates collimate the fiber-outputs and deliver circularly polarized expanded light-beams to the MOT. For normal operation a sufficient power-level of cooling light in each beam is 18 mW, and the detuning relative to the cyclic $|^2S_{1/2}, F = 2\rangle \rightarrow |^2P_{3/2}, F = 3\rangle$ cooling-transition is -23 MHz. The $|^2S_{1/2}, F = 1\rangle \rightarrow |^2P_{3/2}, F = 2\rangle$ repump light is primarily present in one of the counter-propagating pairs, and the typical measured power level here is 2×1 mW.

One pair of the movable quadrupole trap-coils (detailed in section 2.3) is used at low current (16 A, radial field gradient $5.76\,\mathrm{G/cm}$) to provide the magnetic field for the MOT. During the last 35 ms of the MOT phase we compress the MOT by detuning the cooling lasers. This is to minimize heating when the magnetic trap is turned on [25].

After the compressed MOT phase, the quadrupole field is briefly turned off, and a separate coil-pair in a Helmholtz-like configuration is pulsed on to provide a uniform bias-field. Under this field atoms are pumped into the $|F = 2, m_F = 2\rangle$ dark-state by a separate σ^+ polarized "pump-laser" beam tuned to the $F = 2 \rightarrow F' = 2$ transition. Ramping the current in the quadrupole-coils up to 250 A catches around 90 % of the atoms (see Fig. 2.3) in the magnetic QP-trap, and immediately after this the transport into the low-pressure region begins.

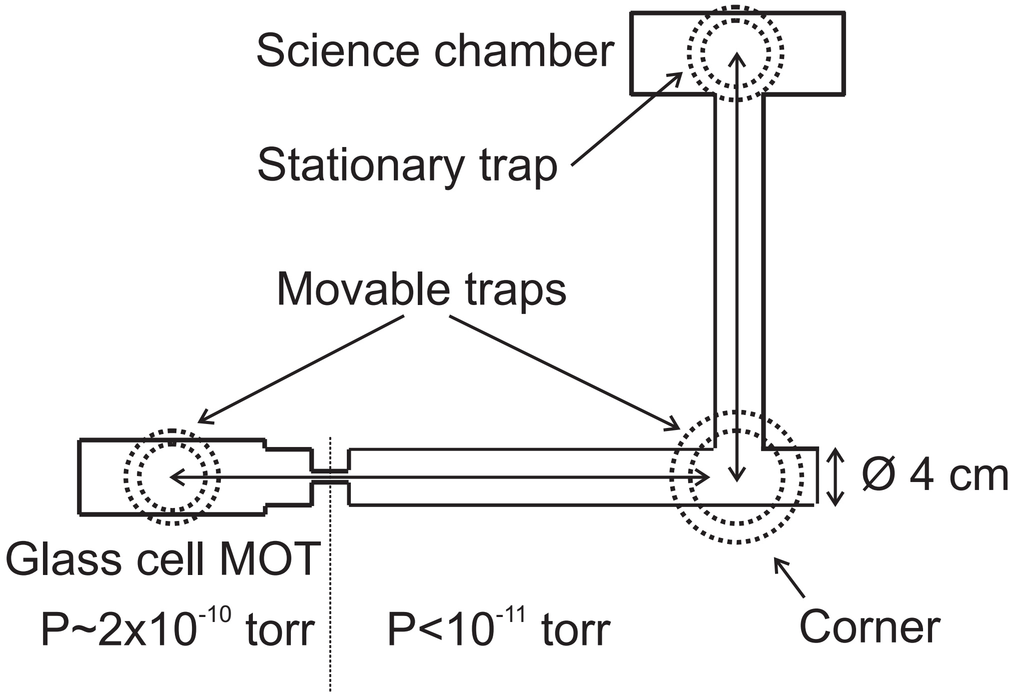

Figure 2.2: Sketch of our glass-cell MOT and steel vacuum chamber. The coils constituting the magnetic traps are symbolized by the dashed circles. The distances from the MOT to the corner and from the corner to the science chamber are 49 cm and 37 cm, respectively.

After several years of operation under undisrupted vacuum conditions, the originally installed rubidium dispensers are now running dry. It has thus become relevant to extend the previous 8-10 sec MOT loading time considerably, so that a change of dispensers can be postponed to coincide with an upcoming moving of the lab.

An unexplained experimental observation was, however, that a long MOT load time, despite reaching a similar MOT-fluorescence level, would lead to smaller BECs. The problem turned out to be that a load-time dependent hysteresis effect in an electro-mechanical shutter delayed the cutoff of cooling light by more than 1 ms. For now, the issue has been fixed by leaving a larger time-gap between cooling cutoff and optical pumping, but in the long term it is expected that the problem will be resolved by replacing the home-built shutter-drivers with Uniblitz drivers matching the shutters in use.

Another experimental oddity is that the pressure-reading derived from the ion-pump current (Varian Star-Cell w. Dual Ion Pump Controller) has risen by two orders of magnitude over the last years. In 2007 the pressure-reading for

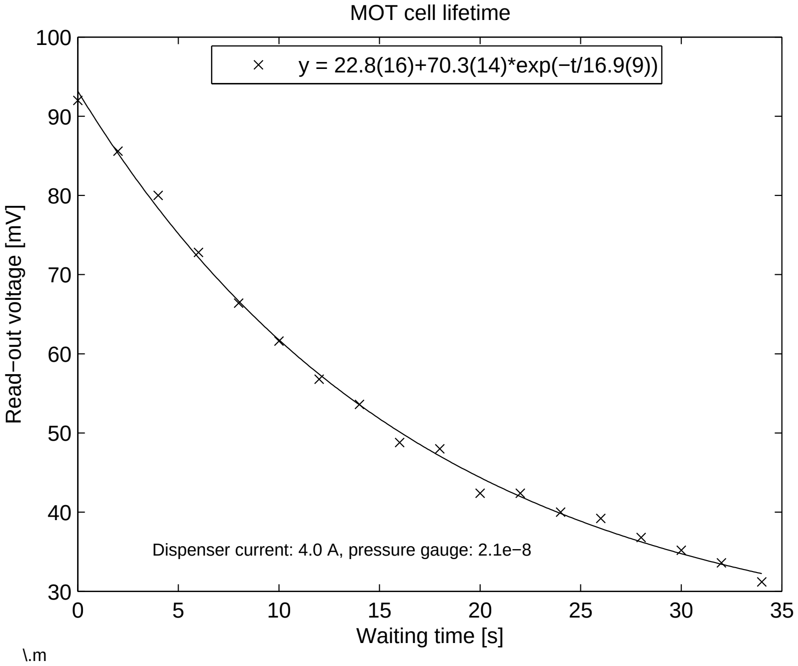

Figure 2.3: Fluorescence signal at recapture in MOT after variable hold time in a purely magnetic QP trap in the MOT region. The data shows a MOT-cell lifetime of 17 seconds (due to background gas collisions). The experimental sequence is triggered by a 100 mV MOT fluorescence photodetector signal, and the 22.8 mV offset is due to reflected cooling-light. The QP-trap capture efficiency is thus 91%.

the MOT section was initially 2×10^{-10} torr. Since then it has increased: First by a factor of 10 in 2008 as noted in [2], and since by another factor of 10, which initially went unnoticed. The increased reading cannot reflect the real pressure, however, as the measured lifetime of atoms held in the magnetic trap has actually increased considerably since 2007. Current lifetime measurements for magnetically trapped atoms in the MOT-cell region yield 17 seconds (see Fig. 2.3), which increases to 21 seconds when turning the dispenser heating current off. This is consistent with a simple rate-equation description of the MOT fluorescence level, which is observed to rise toward its saturation level on a similar time-scale. An in depth investigation of the actual pressure would thus probably reveal the *opposite* conclusion, namely that the pressure in the MOT chamber has in fact fallen since 2007.

2.3 Transport with Movable Quadrupole Traps

The two movable magnetic quadrupole traps are mounted on computer controlled mechanical positioning systems similar to [25]. One QP-trap (the MOT-QP) moves the atoms from the MOT to the corner of the chamber while the other (the Conveyor QP) moves them from the corner to the science chamber (see sketch in Fig. 2.2). Mounted directly on the science chamber is a third pair of QP-coils and a smaller Ioffe coil, which together provide the trapping field during evaporative cooling.

The atoms are trapped using the linear Zeeman shift, which for a magnetic field of magnitude $B(\mathbf{r})$ provides the trapping potential

$$V(\mathbf{r}) = g_{\mathrm{F}}\, m_{\mathrm{F}}\, \mu_B\, B(\mathbf{r}) \tag{2.1}$$

where $g_{\mathrm{F}} = -1/2$ for the $F = 1$ hyperfine state and $g_{\mathrm{F}} = 1/2$ for the F=2 hyperfine state of the electronic $^2S_{1/2}$ groundstate of ^{87}Rb. The "low-field seeking" states $|F = 1, m_F = -1\rangle$, $|F = 2, m_F = 1\rangle$ and $|F = 2, m_F = 2\rangle$ are thus potentially trappable.

The quadrupole traps can be approximated by two circular current loops with radius R and separation distance 2A. Around the zero-point in the middle of the trap the magnetic field increases linearly in all directions with the axial gradient being twice the radial gradient. Near the minimum the magnitude of the magnetic field can thus be well approximated by [29]

$$B(\rho, z) \approx \frac{\partial |B|}{\partial \rho} \sqrt{\rho^2 + 4z^2} \tag{2.2}$$

where $\partial |B| / \partial \rho$ is the radial magnetic field gradient.

The magnetic field from our coils can be calculated using a numerical implementation of the Biot-Savart law. These calculations show that for our purposes, the magnetic field from the coils can be very accurately approximated by the field from two circular windings with axial distance A, radius R and current-scaling I. Comparing with the numerical code, the best fitting values for A, R, I, and the associated field gradient and barrier height, are listed in table 2.1.

The maximum current we can use in our coils is 400 A which is limited by the current supply, but presently no experimental sequence is using more than 300 A in any coil.

Similarly to the movable coils, the Ioffe and quadrupole coils, mounted directly on the science chamber, are cast in epoxy for mechanical stability. Together they form a Quadrupole-Ioffe configuration (QUIC) trap [16], which

Coil	MOT QP-trap	Conveyor QP-trap
A_{fit}(cm)	3.941	7.082
R_{fit}(cm)	3.2	4.21
I_{fit}(A/A)	16.0	32.17
Radial field gradient (G/(cm A))	0.36	0.20
Field barrier height (G/A)	0.77	0.59

Table 2.1: Quadrupole coil parameters

we transform from QP to QUIC configuration by ramping the Ioffe coil current from zero (bypassed) up to the full QP current, at which point the Ioffe and QP-coils form a series circuit.

The measured turn-off time of the QUIC current is 260 μs, but residual eddy-currents in the chamber walls die out on a slightly longer (millisecond) time-scale. For BEC imaging with long time-of-flights (TOF), e.g. $\text{TOF} > 10$ ms, there is, however, no sign of residual induced fields.

2.4 Evaporative Cooling

The creation of BECs by standard forced radio-frequency evaporative cooling is well described in the literature [46]. Basically, an RF frequency magnetic field couples the magnetic spin states, causing a transfer from a low-field seeking trapped state to a high-field seeking untrapped state for any atom passing the shell-like set of points $\mathbf{r}$ defined by the resonance condition $h\nu_{\text{RF}} = \mu_B g_F |B(\mathbf{r})|$. By sweeping down the RF frequency, the resonance condition shell gradually shrinks toward the trap center. This process continuously removes the upper tail of the motional energy distribution of the atoms. And if the sweep rate is slow enough to keep the distribution close to equilibrium, this evaporative cooling of atoms will be very efficient.

Due to the aforementioned lack of rubidium in the heatable dispensers, the evaporative cooling sequence has recently been re-optimized in order to make BECs from smaller MOT starting conditions, while making the most of the low background pressure in the science chamber.

To this end, the RF frequency ramp was changed from an exponential ramp to linear ramp segments covering the set of RF frequency intervals shown in the first column of table 2.2. With the frequency intervals fixed, optimization of the sweep times was carried out on all but the first interval by plotting number of atoms and fitted phase-space density. Figure 2.4 shows the phase-space density and atom number scatter for the optimum sweep times given in column 2 of 2.2.

Frequency interval	Sweep time	Run numbers
55 MHz → 15 MHz	8 sec	N.A.
15 MHz → 5.5 MHz	15 sec	57 → 61
5.5 MHz → 2.2 MHz	15 sec	52 → 56
2.2 MHz → 900 kHz	8 sec	47 → 51
900 kHz → 600 kHz	1.25 sec	42 → 46
600 kHz → 385 kHz	1.5 sec	37 → 41

Table 2.2: RF ramp intervals and optimized time-parameters. Experimental run numbers from June 17., 2010.

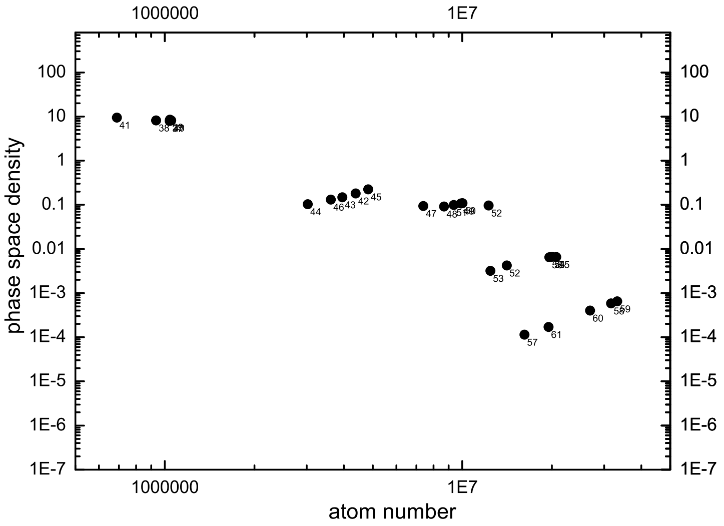

Figure 2.4: Phase-space density plot during evaporation. Points are labeled by their run-numbers on June 17., 2010.

Comparing the run-numbers in table 2.2 and figure 2.4, one sees a significant variation within each group of supposedly identical runs. This is attributed to unstable initial conditions from the MOT.

2.5 Absorption Imaging

The detection method used for all experiments described is standard absorption imaging with beams resonantly tuned to the $|S_{1/2}, F = 2\rangle \rightarrow |P_{3/2}, F' = 3\rangle$ transition [46, 5, 2]. The resolution varies slightly between the different imaging axes, but is on the order of 5 microns with 2 microns/pixel (1.94 microns/pixel on the x-axis camera, which is used exclusively for the data presented here).

Chapter 3

Optical Lattices

3.1 Introduction

Optical lattices provide one of the most important tools used in the study of ultra-cold quantum gases. While being conceptually simple and experimentally accessible, they allow a vast range of interesting and non-trivial physical phenomena to be studied in fairly "clean" experiments.

The basic unifying concept of optical lattice physics is that interference patterns of standing wave laser-fields create a "potential landscape", in which atoms move. For ultra-cold atoms, the thermal de Broglie wavelength is comparable to the wavelength of optical lasers. Even the motional dynamics of ultra-cold atoms in optical lattices are thus within the realm of quantum mechanics.

The all important distinguishing feature of optical lattices, as compared to formally similar systems in e.g. solid state physics, is the extraordinary controllability of the lattice potential:

- The potential scales with the laser intensity, which is easily controlled over a large parameter range and with fast and accurate dynamics.

- The potential shape can be controlled both statically and dynamically by a number of specialized techniques. Transverse shaking of the lattice, acceleration of the lattice and changing the angle between incident laser beams to modify the interference pattern are just a few of the many techniques in common use.

- For atomic species with hyperfine structure, the potential experienced by different $|F, m_F\rangle$ states depends on both laser polarization and relative detuning. Elaborate schemes for e.g. spin-dependent transport make use of this state-dependence of the potential.

Combining the versatility of optical lattices with RF fields (coupling $\langle F, m'_F|H_{RF}|F, m_F\rangle$ states), MW fields (coupling $\langle F', m'_F|H_{MW}|F, m_F\rangle$ states), close to resonance laser fields (coupling to electronically excited atomic states for e.g. molecule formation) and strong B-fields (for Feschbach physics), gives an almost unlimited range of interesting experiments based on optical lattices.

The ongoing theoretical and experimental research based on optical lattices is, however, not solely motivated by its academically appealing nature. One of the more practical reasons for studying lattice physics is that complex solid state systems like high-temperature superconductors are very difficult to analyze theoretically. In this respect optical lattices fulfill two related purposes:

- They provide a well controlled experimental "test-bed" for many-body quantum theory developments.

- And they can be used to realize "quantum simulators", i.e. to implement a well controlled physical model of an interesting physical system. This usage is conceptually similar to the now obsoleted analog computers, but can be justified because ab initio digital simulation of even moderately sized many-body quantum systems is not yet possible with contemporary super-computers.

3.2 AC Stark-shift Induced Potentials

The physical mechanism underlying optical dipole traps and lattices can be explained both classically, semi-classically and in a 'dressed state' picture using second order perturbation theory [21]. Each approach offers a different trade-off between physical intuition and theoretical rigor.

3.2.1 Classical and Semi-Classical Approaches

Consider a neutral atom at position $\mathbf{r}$. In the (semi-)classical approaches, it is observed that an oscillating laser field

$$\mathbf{E}(\mathbf{r}, t) = \hat{\mathbf{e}}\, \tilde{E}(\mathbf{r})\, e^{-i\omega t} + c.c. \tag{3.1}$$

gives rise to an induced atomic polarization

$$\mathbf{p}(\mathbf{r},t) = \hat{\mathbf{e}}\,\tilde{p}(\mathbf{r})\,e^{-i\omega t} + c.c. \tag{3.2}$$

which is approximately linear in the E-field, as described by the frequency dependent complex polarizability α,

$$\tilde{p} = \alpha\tilde{E} \tag{3.3}$$

Although related through Kramers-Kronig relations, the real and imaginary parts of $\alpha(\omega)$ convey information about different physical mechanisms. The imaginary "out-of-phase" response describes the power absorbed (and reemitted spontaneously)

$$\begin{aligned} P_{\text{abs}} &= \langle\dot{\mathbf{p}}\mathbf{E}\rangle && (3.4)\\ &= \frac{\omega}{\epsilon_0 c}\,\mathrm{Im}(\alpha)\,I && (3.5)\end{aligned}$$

while the real "in-phase" response describes the dipole-potential arising from the interaction between induced polarization and E-field,

$$\begin{aligned} U_{\text{dip}} &= -\frac{1}{2}\langle\mathbf{p}\mathbf{E}\rangle && (3.6)\\ &= -\frac{1}{2\epsilon_0 c}\,\mathrm{Re}(\alpha)\,I && (3.7)\end{aligned}$$

Here both P_{abs} and U_{dip} are averaged on a full cycle, and

$$I = 2\epsilon_0 c|\tilde{E}|^2 \tag{3.8}$$

has been substituted to facilitate practical calculations.

A basic property of classical harmonic oscillators is that far below and above resonance, the phase of the response is close to 0 and π, respectively, i.e. a non-dissipative reactive response. In the current context, this implies that for large laser detunings, the dipole interaction can be non-negligible while spontaneous emission is efficiently suppressed. It also quite intuitively explains why red-detuned laser fields give rise to negative potentials, which may trap atoms in intensity peaks, while blue-detuned fields tends to repel atoms from the intensity peaks.

More quantitatively one may derive the approximate results for a two-level system,

$$U_{\text{dip}}(\mathbf{r}) = \frac{3\pi c^2}{2\omega_0^3}\,\frac{\Gamma}{\Delta}\,I(\mathbf{r}) \tag{3.9}$$

$$\Gamma_{\mathrm{sc}}(\mathbf{r}) = \frac{3\pi c^2}{2\hbar\omega_0^3}\left(\frac{\Gamma}{\Delta}\right)^2 I(\mathbf{r}) \tag{3.10}$$

where $\Gamma_{\mathrm{sc}}(\mathbf{r}) = P_{\mathrm{abs}}/(\hbar\omega)$ is the experimentally relevant scattering rate, while Γ is the spontaneous decay rate and Δ is the laser detuning. By letting both detuning Δ and intensity $I(\mathbf{r})$ become large, it follows immediately that the scattering rate can be made arbitrarily low for a given potential depth.

Inserting numbers, one may verify that for e.g. ^{87}Rb, where $\Gamma \approx 2\pi \cdot 6$ MHz [43], it is in principle fully feasible to realize trap depths on the order of micro Kelvin, with spontaneous scattering rates on the order of 10^{-3} Hz. Practical traps are, however, limited by other heating mechanisms on a shorter timescale [40].

For later reference, it is noted that the spontaneous decay rate, Γ, is related to the electric dipole operator matrix element through

$$\Gamma = \frac{\omega_0^3}{3\pi\epsilon_0\hbar c^3}|\langle e|\hat{\mu}|g\rangle|^2 \tag{3.11}$$

but it may also be estimated classically.

3.2.2 Dressed State Picture

A quantitative treatment of the induced dipole potential should take into account both the fine and hyperfine level splittings of the ground and excited states, instead of the above two-level description. In this case it proves advantageous to do a second order perturbative treatment of the energy shifts of the combined atom and field system.

The non-degenerate second order perturbative energy shift is

$$\Delta E_i = \sum_{j\neq i}\frac{|\langle j|H_I|i\rangle|^2}{E_i - E_j} \tag{3.12}$$

where the interaction Hamiltonian $H_I = -\hat{\mu}\mathbf{E}$ is given in terms of the electric dipole operator $\hat{\mu}$.

Starting with a two-level atom with levels $|g\rangle$ and $|e\rangle$, the relevant non-interacting 'dressed' states are $|g,n\rangle$ and $|e,n-1\rangle$, having n and $n-1$ field quanta respectively. The difference between the corresponding dressed state energies is given by the detuning, $E_g - E_e = \hbar\Delta$. The energy-shift for the ground state thus becomes*

$$\begin{aligned}\Delta E_g &= \frac{|\langle e|\hat{\mu}|g\rangle|^2}{\hbar\Delta}|E|^2 && (3.13)\\ &= \frac{3\pi\epsilon_0 c^3}{\omega_0^3}\frac{\Gamma}{\Delta}|E|^2 && (3.14)\\ &= \frac{3\pi c^2}{2\omega_0^3}\frac{\Gamma}{\Delta}I && (3.15)\end{aligned}$$

using (3.11) and (3.8). It is noticed that this perturbative energy-shift of the dressed atom ground-state is identical to the (semi-)classical dipole interaction potential given in (3.9).

Extrapolating the very reasonable correspondence between the optical dipole potential and the dressed state AC Stark-shifts, one may now also calculate the optical dipole potentials for the plethora of fine and hyperfine levels in real alkali atoms using dressed-state perturbation theory. While the basic procedure is to include the additional states and coupling-terms in (3.12), additional simplifications arise from the fact that all the involved dipole operator matrix-elements are expressible in a single reduced dipole matrix-element, corresponding to the spin independent electric dipole coupling of electronic orbital states.

The simplifying sum-rules of the involved Wigner 6-j symbols and Clebsch-Gordan coefficients are outside the scope of this thesis. The end results may, however, be classified according to whether the detuning is large or small with respect to the fine and hyperfine structure splittings.

At intermediate detuning with resolved excited state fine-structure, but unresolved excited state hyperfine-structure, $|\Delta| \gg \Delta'_{\mathrm{HFS}}$, the dipole potential is found to be

$$U_{\mathrm{dip}}(\mathbf{r}) = \frac{\pi c^2 \Gamma}{2\omega_0^3}\left(\frac{2+\mathcal{P}g_F m_F}{\Delta_{2,F}} + \frac{1-\mathcal{P}g_F m_F}{\Delta_{1,F}}\right) I(\mathbf{r}) \qquad (3.16)$$

Here $\mathcal{P} = \{0, \pm 1\}$ corresponds to linearly or circularly polarized light, while $\Delta_{2,F}$, $\Delta_{1,F}$ are the detunings corresponding to the transitions between the relevant F hyperfine groundstate and the centers of the hyperfine-split $P_{3/2}$ and $P_{1/2}$ excited states (the D_2 and the D_1 line).

At large detuning with unresolved fine-structure, $\Delta \gg \Delta'_{\mathrm{FS}}$, the dipole potential is found to be

$$U_{\mathrm{dip}}(\mathbf{r}) = \frac{3\pi c^2}{2\omega_0^3}\frac{\Gamma}{\Delta}\left(1 + \frac{1}{3}\mathcal{P}g_F m_F \frac{\Delta'_{\mathrm{FS}}}{\Delta}\right) I(\mathbf{r}) \qquad (3.17)$$

---

*Since $\hat{\mu}$ is actually a vector operator, an implicit assumption about the E-field polarization is made here.

Here Δ is the detuning with respect to the center of the D-line doublet (neglecting the hyperfine structure completely). At very large detunings, as used in our experimental setup, this expression is identical to the semi-classically derived result (3.9).

There are, however, two important issues to keep in mind with the above results. Firstly, as pointed out explicitly in [21], the use of *non-degenerate* second order perturbation theory is only valid for purely linear π or circular $\sigma^{\pm}$ polarizations, since in this case no coupling exist between the degenerate ground-states. For mixed polarizations, Raman couplings between the degenerate ground-states are present, and the above procedure fails.

Secondly, the rotating wave approximation has been used throughout. In settings where $\Delta \ll \omega_0$, this is fully justified. In our laboratory setup, however, the resonant transition is at 780 nm, while the lattice lasers operate at 914 nm. Since the AC Stark-shift is proportional to $1/\Delta$, the relative strength of the neglected potential terms are thus expected to be on the order of

$$\begin{aligned} \frac{|\Delta_{\text{co}-\text{rotating}}|}{|\Delta_{\text{counter}-\text{rotating}}|} &= \frac{914-780}{914+780} && (3.18) \\ &\approx 8\% && (3.19) \end{aligned}$$

which is a quite significant correction.

3.3 Lattice Band Structure

In optical lattices the AC Stark shift is used to create a periodic potential, and the simplest realization consists of two counter-propagating laser beams of identical amplitude and linear polarization. The plane-wave laser fields,

$$E_{\pm} = \hat{\mathbf{e}}\, \tilde{E}\, e^{i(\mathbf{kx} \mp \omega t)} + c.c. \tag{3.20}$$

gives rise to a standing wave interference pattern,

$$\begin{aligned} \langle |E_+ + E_-|^2 \rangle &= 4|\tilde{E}|^2 + 2\,\tilde{E}^2\, e^{i2\mathbf{kx}} + 2\,\tilde{E}^{*2}\, e^{-i2\mathbf{kx}} && (3.21) \\ &= 4|\tilde{E}|^2 \big(1 + \cos(2\mathbf{kx})\big) && (3.22) \end{aligned}$$

where $\tilde{E}$ is assumed real in the last step. The spatial modulation at $2\mathbf{k}$ is our prime interest here, since the associated AC Stark shift gives rise to a modulated atomic dipole potential. By adding more counter-propagating laser beams, the lattice modulation can be extended from 1 to 2 or 3 dimensions.

In order to analyze the behavior of a BEC in such an optical lattice, we shall not only make the usual mean-field approximation [38], but also neglect the non-linear interaction term in the resulting Gross-Pitaevskii equation. In this limit, the whole condensate is thus described by the single-particle Schrödinger equation for each individual atom

$$\left(\frac{-\hbar^2}{2M}\nabla^2 + V(\mathbf{r})\right)\Psi(\mathbf{r}) = E\,\Psi(\mathbf{r}) \tag{3.23}$$

3.3.1 Reciprocal Space Bloch Theorem

Just as in the theory of crystalline solids, the periodicity of $V(\mathbf{r})$ implies a particular "Bloch-Floquet" form of the eigenstate solutions. To see this explicitly, consider that in reciprocal space multiplication is convolution. The k-space Schrödinger equation is thus

$$\frac{\hbar^2\mathbf{k}^2}{2M}\tilde{\Psi}(\mathbf{k}) + \frac{1}{\sqrt{2\pi}}\left(\tilde{V} * \tilde{\Psi}\right)(\mathbf{k}) = E\,\tilde{\Psi}(\mathbf{k}) \tag{3.24}$$

For a general 3D periodic potential $V(\mathbf{r}+\mathbf{R}_i) = V(\mathbf{r})$, where $\mathbf{R}_i$ are the crystal-vectors spanning a unit cell, the k-space potential takes the form of a reciprocal lattice

$$\tilde{V}(\mathbf{k}) = \sum_{n_i,n_j,n_k} V_{n_in_jn_k}\delta^{(3)}(\mathbf{k} - n_i\mathbf{K}_i - n_j\mathbf{K}_j - n_k\mathbf{K}_k) \tag{3.25}$$

with $\mathbf{K}_i \cdot \mathbf{R}_j = 2\pi\delta_{ij}$.

We now make the ansatz that the k-space wave-function is defined on a similar reciprocal lattice with an offset $\mathbf{q}$,

$$\tilde{\Psi}_{\mathbf{q}}(\mathbf{k}) = \sum_{n_i,n_j,n_k} \Psi_{\mathbf{q}n_in_jn_k}\delta^{(3)}(\mathbf{k} - \mathbf{q} - n_i\mathbf{K}_i - n_j\mathbf{K}_j - n_k\mathbf{K}_k) \tag{3.26}$$

From (3.24) and (3.25) it follows that the offset reciprocal lattice forms a closed subspace where (3.24) can be diagonalized. This, in turn, justifies the ansatz.

The offset, $\mathbf{q}$, of the k-space grid corresponds to the phase-factor in the more common direct-space formulation of the Bloch-theorem,

$$\Psi(\mathbf{r}) = e^{i\mathbf{q}\cdot\mathbf{r}}\,u(\mathbf{r}) \tag{3.27}$$

$$u(\mathbf{r}+\mathbf{R}_i) = u(\mathbf{r}) \tag{3.28}$$

3.3.2 The 1D Lattice Band-Structure

For the 1D lattice, the numerical diagonalization proceeds as follows. Since only discrete k-values corresponding to points on the offset reciprocal lattice are of interest, we change free variable from k to the discrete index n. The Schrödinger equation then reads

$$\frac{\hbar^2(q+nK)^2}{2M}\Psi_q(n)+\sum_m V(n-m)\Psi_q(m)=E_q\,\Psi_q(n) \tag{3.29}$$

where $\Psi_q(n)$ and $V(n)$ are vectors of discrete Fourier coefficients for $u(x)$ and the potential $V(x)$. For $V(x)=(V_0/2)\cos(Kx)$, as in an optical lattice, the expression simplifies to

$$\frac{\hbar^2(q+nK)^2}{2M}\Psi_q(n)+\frac{V_0}{4}\big(\Psi_q(n-1)+\Psi_q(n+1)\big)=E_q\,\Psi_q(n) \tag{3.30}$$

Finally, expressing q in units of the recoil wavenumber $k_r=K/2$ (i.e., the wavenumber of the lattice light, $k_r=2\pi/\lambda$), and E_q and V_0 in units of recoil energy, $E_r=\frac{\hbar^2k_r^2}{2M}$, the numerical eigenvalue equation reads

$$(q+2n)^2\Psi_q(n)+\frac{V_0}{4}\big(\Psi_q(n-1)+\Psi_q(n+1)\big)=E_q\,\Psi_q(n) \tag{3.31}$$

which can be solved numerically as a tri-diagonal matrix eigenvalue problem by truncating at finite n. In figure 3.1 the 3 lowest eigenvalues are plotted for $q\in(-k_r,k_r)$, i.e. the first Brillouin-zone. The lattice depth used for the figure is $V_0=2E_r$, and for comparison the free-particle dispersion curves are also plotted.

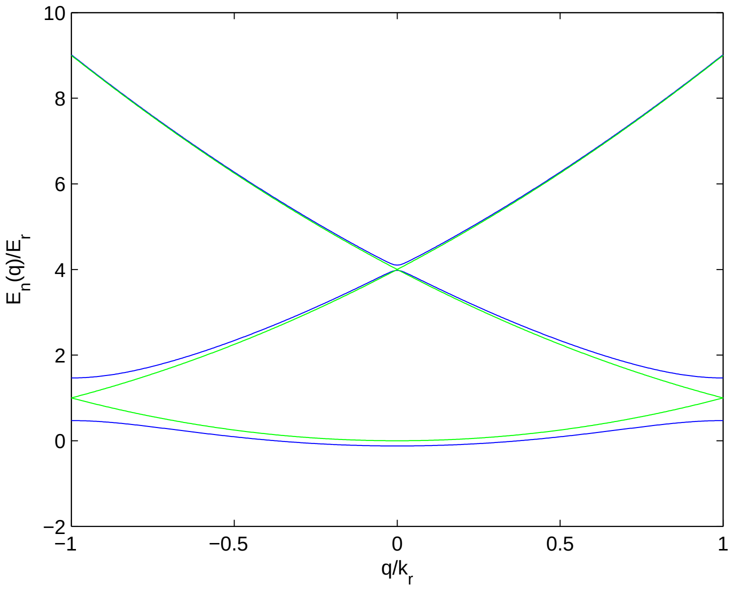

Figure 3.1: Band-structure (blue) and free particle dispersion curves (green). The lattice depth is $V_0 = 2E_r$, and the numerical representation is truncated to 40 discrete Fourier-components.

Chapter 4

Lattice Calibration Techniques

The main results of this chapter are to be published in [37].

4.1 Introduction

The investigation of ultracold atomic samples in optical lattice potentials is of vast interest, since it allows for a new experimental approach to study strongly correlated lattice systems. The research field has therefore expanded rapidly over the past years and both the static [7] and dynamic properties [31] of ultracold atoms in optical lattices have been investigated in detail. However, the precise determination of the lattice depth remains a cumbersome and time-consuming task in most experiments.

A number of common calibration techniques were developed in early work [13, 10] using 1D lattices and a summary was provided in [31]. These techniques have been refined in more recent work [18]. Here we demonstrate the use of Kapitza-Dirac scattering, Landau-Zener tunneling and parametric excitation for optical lattice depth calibration.

The starting point for the experiments reported in this chapter is a Bose-Einstein condensate with about 3×10^5 rubidium atoms in the $F = 2, m_F = 2$ state, held in a magnetic QUIC trap. The trap frequencies are 12.3 Hz in the axial (horizontal) direction, and 37.9 Hz in radial directions (see Fig. 4.1). Along the vertical direction a lattice is formed by a $\lambda = 914$ nm retro-reflected laser beam with a $1/e^2$ waist of 120 μm. After a variable interaction time Δt, the condensate is released and images are taken after time-of-flight.

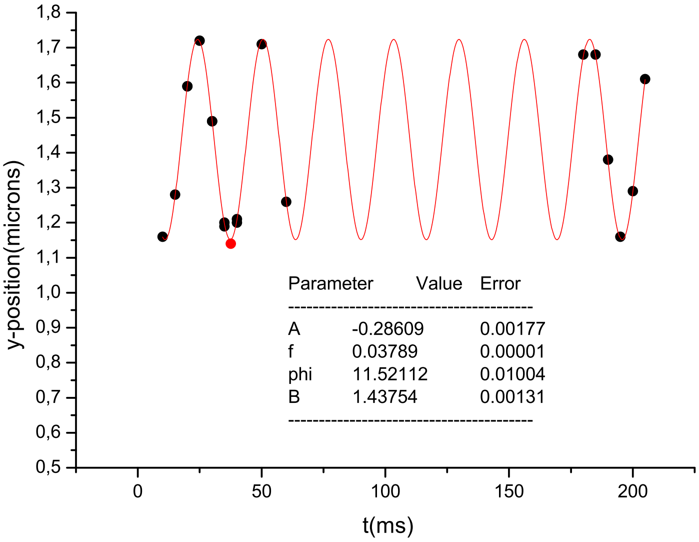

Figure 4.1: Measurement of the radial frequency in the QUIC trap configuration. The motion is initiated by a sudden change of trap current.

4.2 Kapitza-Dirac Scattering

Kapitza-Dirac scattering of a BEC by an optical lattice was first reported in 1999 [35]. The atomic diffraction pattern thus obtained with short standing-wave pulses is frequently used for the lattice depth calibration [13, 41, 42, 32] due to its high accuracy.

When a standing wave of short duration and constant amplitude is applied to a condensate, its time-of-flight images show diffracted patterns, where the population in each momentum component displays oscillatory behavior. The physical mechanism behind the seemingly complex observed interference phenomenon is conceptually very simple, as outlined below.

Before turn-on of the lattice pulse, the mean-field condensate wave-function is in the ground state, i.e. a Gaussian in the limit of vanishing interaction, or an inverted parabola in the Thomas-Fermi approximation [38]. In the following, we stick to the non-interacting model.

Approximating the lattice turn-on as an instantaneous change of trapping-potential, we project the initial wave-function onto the energy eigenstates of the new potential. As the initial wave-function spans a large number of individual lattice sites and has constant phase, the projection onto the Bloch-eigenstates will only populate a narrow range of quasi-momenta, $\hbar q$, around $q = 0$. Eigenstates from multiple bands will, however, contribute. Since all of these states have different energy, the time evolution of the system during the pulse-time, Δt, is given by phase-factors, $\exp(-iE_m(q \approx 0)\Delta t/\hbar)$ for each component.

At the end of the lattice pulse, the resulting state is projected onto plane waves, i.e. momentum eigenstates. And as the magnetic trapping potential is turned off at the same time, the amplitude of the projection onto each of these plane-wave momentum-eigenstates is directly mapped to the real-space position by the evolution during time-of-flight. It is important to recognize that each $|m, q \approx 0\rangle$ state will project onto multiple $p_n = 2n\hbar k_r$ states. And, vice versa, each of the observed p_n components will in general contain contributions from multiple bands, and thus display complex oscillatory behavior corresponding to the relative phase evolution of the bands.

For shallow lattice-depths and short enough pulse durations, the effect of the periodic lattice potential is just to modify the phase, but not the amplitude, of the mean-field wave function. The momentum distribution in this "thin grating" limit can be expressed by Bessel functions [35].

For longer, but weak pulses, the momentum distribution is found to display simple oscillations. In the band-structure picture used here, this is because the initial projection primarily populates states $|m = 0, q \approx 0\rangle$ and $|m = 2, q \approx 0\rangle$, i.e. band 0 and 2, while the first band is not populated due to parity.

For deeper lattices the higher bands become important, and the evolution of each $p_n(\Delta t)$ component must be calculated numerically. The non-periodic oscillations of $p_n(\Delta t)$ can thus be used for calibration without any lattice depth limit, provided that a fast numerical 1D band-structure calculation is used within in the fit routine.

To examine the deep lattice Kapitza-Dirac scattering experimentally, the lattice pulse is applied to the BEC for a duration Δt. The lattice and magnetic trap are then turned off simultaneously, and the BEC is allowed to expand freely for 14 ms. After the expansion, we take absorption images showing clearly separated momentum components $p_n = 2n\hbar k_r$.

For each scattering order n, we measure the atom number N_n. In figure 4.2 we plot N_n/N_T vs Δt (N_T is the summed total atom number) and comparing with the numerically fitted band-structure calculation (solid curves), we find that all orders give the same value of the lattice depth, here $V_0 = 40.8E_r$. In this way, we can determine the correspondence between the signal from a photo-detector probing a sample of the lattice beam, and the actual lattice depth. The Kapitza-Dirac scattering method is thus a fast and reliable tool for lattice depth calibration, which covers a broad range of lattice depth regimes.

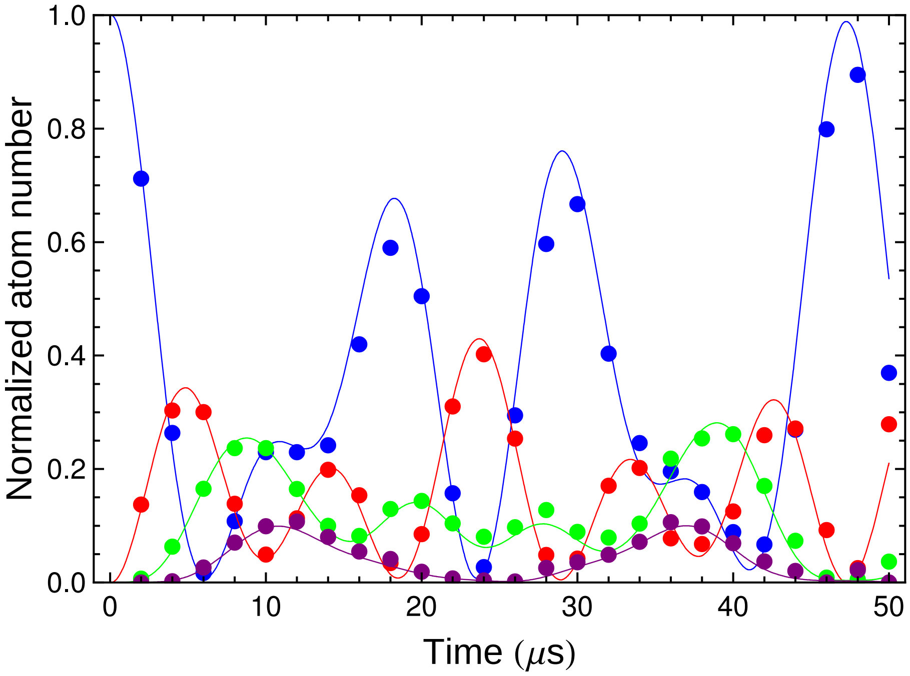

Figure 4.2: Time evolution of each momentum component as a function of Kapitza-Dirac pulse duration (Δt). Blue, red, green, and purple correspond to the momentum order $n = 0, 1, 2, 3$, and 4, respectively. All momentum components give the same result for the optical lattice depth.

4.3 Bloch Oscillation and LZ-Tunneling

Coherent splitting of a condensate by Landau-Zener (LZ) tunneling can occur when matter waves are accelerated in an optical lattice, and Bloch oscillation of the non-tunneling fraction even allows multiple consecutive splittings to occur at regular intervals [3]. Morsch *et* al. [30] loaded BECs of rubidium atoms into a shallow optical lattice that was subsequently accelerated by chirping the frequency difference between the lattice beams. From the resulting interference pattern, the condensate group velocity in the frame of reference of the lattice was calculated and plotted against the lattice velocity, clearly showing the Bloch oscillations. They also demonstrated LZ tunneling as a tool for measuring the optical lattice depth as well as the effects of the mean-field interaction between the atoms in the condensate [10]. Recently, Bloch oscillations of condensates in a vertical lattice are being used in the context of atom interferometry [17, 22].

4.3.1 Bloch Oscillation

When a matter-wave packet with narrow quasi-momentum distribution around $q(t)$ is subjected to a constant uniform external force, the quasi-momentum will increase similarly to the momentum of a free particle. In the case of gravitational acceleration, g, of an atom with mass m, the quasi-momentum is thus [31]

$$\hbar q(t) = \hbar q_0 + mgt \tag{4.1}$$

At the edge of the Brillouin-zone ($q = k_r$), the periodic lattice potential fulfills the condition for Bragg-reflection of the wave-packet into $q = -k_r$. In the band-structure picture, one may think of the same physical process as an adiabatic following at the avoided crossing of the bands. For vanishing lattice depth, the band-structure is identical to the free-particle dispersion curve, and there is no energy-gap between any of the bands crossing at $q = \pm k_r$ (or at $q = 0$ for higher bands). For increasing lattice depth, however, avoided crossings of the energy-bands appear. The lowest band-gap can be seen clearly in figure 3.1, while the higher band-gaps open at increasing lattice depths. For increasing gap width compared to the acceleration, the probability that the particle will make an adiabatic "jump" from one band to another, instead of continuing the Bloch cycle in the same band, diminishes.

4.3.2 Landau-Zener Theory

To analyze the transition probability between the bands, an approximative time-dependent Hamiltonian description can be used. One of the few exactly solvable systems involving time-dependent Hamiltonians is the classic two-level crossing Landau-Zener problem,

$$H(t) = \frac{\hbar}{2}\begin{pmatrix} \alpha t & \Omega \\ \Omega & -\alpha t \end{pmatrix} \tag{4.2}$$

where α and Ω are real constants. For small band-gaps, this models the avoided crossings occurring in the band-structure picture, while for larger gaps, the non-linearity of the bands becomes significant.

The Hamiltonian (4.2) is defined in the *diabatic* basis, whose energy eigenvalues cross for $\Omega = 0$, and are given by $E_{diab} = \pm\frac{\hbar}{2}\alpha t$. For $\Omega \neq 0$, the time-dependent *adiabatic* eigenvalues are

$$E_{adiab} = \pm\frac{\hbar}{2}\sqrt{\Omega^2 + \alpha^2 t^2} \tag{4.3}$$

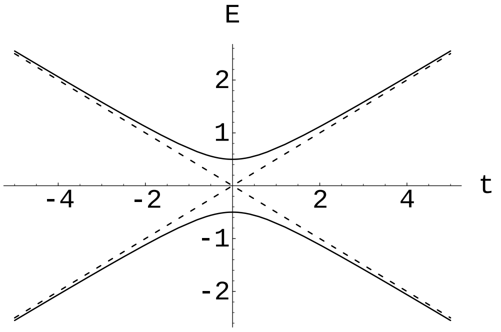

Figure 4.3: General form of an avoided two level crossing with adiabatic levels (solid) and diabatic levels (dashed). Dimensionless, $\Omega = \alpha = \hbar = 1$.

The avoided crossing of the adiabatic levels, and the crossing diabatic levels are shown schematically in figure 4.3.

If $\Omega^2/\alpha \gg 1$, i.e. if the system changes slowly or the coupling is large, the probability of a "jump" across the avoided crossing gap, from one adiabatic level to the other, is vanishing. The system state instead follows the adiabatic curves. In the other limit, $\Omega^2/\alpha \ll 1$, the system will follow the diabatic levels and jump across the gap.

The probability, p, that a system prepared in a particular adiabatic state at $t = -\infty$ will make a non-adiabatic transition and be found in the other adiabatic state (i.e. the same diabatic state) at $t = \infty$ is [45, 44]

$$p(\infty, -\infty) = e^{-\pi\Omega^2/(2\alpha)} \tag{4.4}$$

This simple result can be derived by means of contour integration, without actually solving the time-dependent Schrödinger equation explicitly [48].

In the context of optical lattice band-structure, the analytical result from the Landau-Zener model can be used to describe the dynamics of accelerated lattices.

4.3.3 Experimental Verification of the Landau-Zener Model

To study the splitting by LZ tunneling, we switch off the magnetic trap and let the atoms evolve in the combined lattice and gravitational potential. Ideally this should map a large part of the wave-function onto the $q \approx 0$ states of the lowest band, which would then undergo quasi-momentum evolution as described above. In reality, some practical problems occur.

While turning off the magnetic QUIC-trap, induced currents in chamber walls and other nearby metallic objects can have a significant influence on the

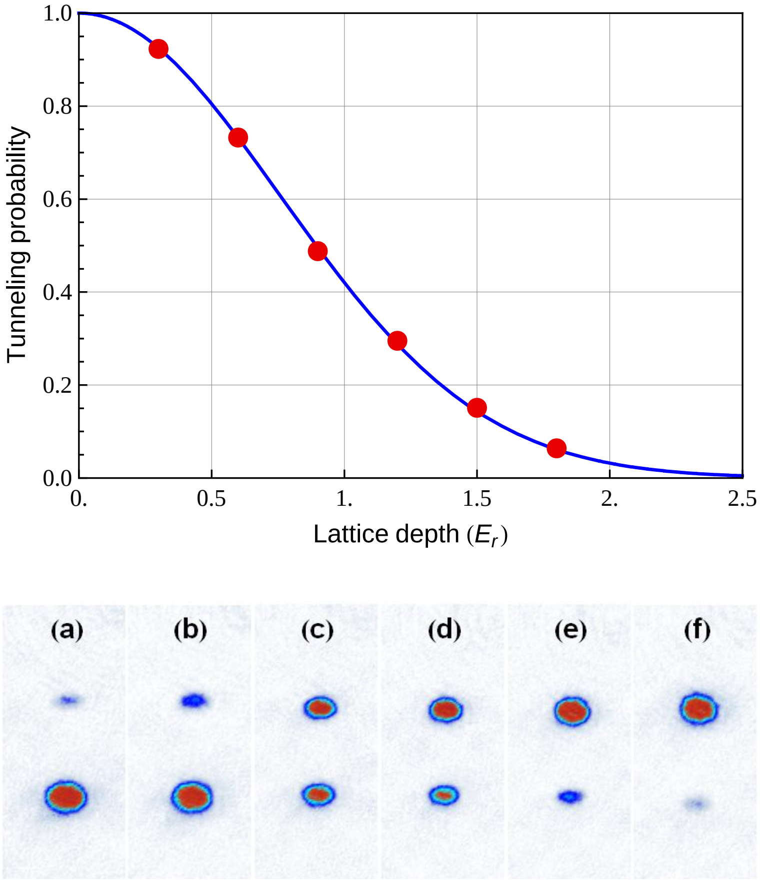

Figure 4.4: Landau-Zener tunneling between the two lowest energy bands of a condensate in an optical lattice as a function of the lattice depth. The blue solid line is the curve from Eq. (4.6) and the dots correspond to the experimental images shown below in (a)-(f)

magnetic field gradient at the trap center. In particular, there may be an asymmetry between the currents induced in metallic objects near the upper and lower quadrupole coil, respectively, as witnessed by the following example:

Few cm above the upper QP-coil in the QUIC trap, there is an aluminum bread-board with a hole for the vertical imaging and lattice light. The board was installed when implementing the optical lattices, but it soon became apparent that it would act as a low-resistance inductive circuit with a calculated time-constant of several milliseconds. Due to its placement close to the upper QP-coil, the inductive coupling was strong, and experimentally it was found to impart a large Zeeman-broadening on the optical transition used for imaging, even in 10 ms time of flight experiments. An easy, and sufficient, solution was to cut a slit in the bread-board to open the loop-circuit.

In the current setup, the temporary field asymmetry during QUIC turnoff seems to be the opposite: A small but significant upward momentum-kick results from the trap turnoff. The interpretation is that induced currents in the vicinity of the lower QP-coil create a gradient in the B-field amplitude, which in turn accelerate the atoms very briefly in the upward direction. In order to load the trapped condensate wave-function into the lowest lattice-band, one can thus either wait until the vertical momentum of the released condensate becomes zero, before (semi-adiabatically) ramping up the lattice power. Or, alternatively, turn on the lattice adiabatically while still in the magnetic QUIC trap, and use a sufficient lattice-depth to suppress any LZ tunneling out of the lowest band during the QUIC turnoff.

The experiments presented in the next chapter use the former method, while here the latter approach is used with an initial lattice depth of 2.4 E_r. In this way we initiate well defined Bloch oscillations in the lowest band. The period of the oscillation is given by

$$\tau_{\mathrm{B}} = \frac{2\hbar k_r}{mg} \tag{4.5}$$

where g is the gravitational acceleration and m is the ^{87}Rb mass, resulting in τ_{B} close to 1 ms.

If the condensate is subjected to the acceleration a and crosses the band gap Δ at the Brillouin-zone edge, the analytical tunneling probability from LZ-theory is

$$r = \exp\left(-\frac{a_c}{a}\right) = \exp\left(-\frac{\lambda\Delta^2}{8\hbar^2 a}\right) \tag{4.6}$$

where a_c is the critical acceleration and a is gravitational acceleration in our experiment.

During the first Bloch oscillation period, the lattice depth is ramped down, so that a chosen fraction of the condensate tunnels to the second band when the quasi-momentum reaches the edge of the Brillouin-zone. Since higher band-gaps are much narrower, the atoms that tunnel to the second band are essentially free, and can be seen as the lower components in Fig. 4.4 (a) to (f).

The other fraction is Bragg reflected as described above. During the next 1 ms Bloch period, the lattice is then ramped down completely, releasing also the reflected fraction. These atoms are visible as the upper components in figure 4.4 (a) to (f).

The tunneling propability is measured directly from the number-ratio of the split condensates, rather than measuring the number of atoms that remain trapped after some multiple of the Bloch period τ_B [10]. We find that with the lattice depth independently calibrated using Kapitza-Dirac scattering, the observed splitting ratio is in good agreement with LZ theory, as shown by the solid curve in figure 4.4.

4.4 Lattice Modulation

A third method of measuring the lattice depth is by direct modulation of the lattice amplitude. This method is only useful in a regime where the lattice is deep enough to support atoms against gravity in both band 0 and band 2.

After loading the BEC into the optical lattice, the magnetic trap is turned off. The lattice amplitude is modulated to excite the atoms from the lowest band (band 0) to the second excited band (band 2) for a time scale of a few milliseconds. A set of images are taken in a certain time after the modulation is finished. Deep lattice depths leads to the regime of 2D pancake shaped condensates where tunneling between adjacent lattice sites is suppressed. In this case, the images of the atomic cloud in the optical lattice are taken at various holding times which show that the atoms are trapped in the lattice against gravity. Even though the lattice depth is deep enough to hold atoms in both bands, a small fraction are heated to even higher bands by the modulation, and fall out of the lattice by tunneling.

For the purpose of detecting the population in the excited band, the magnetic and the lattice potential are switched off to perform time-of-flight experiments. By making the lattice turn-off an adiabatic ramp (while still taking less than τ_B), the second band population is mapped to the $p = \hbar(q \pm 2k_r)$ momentum components, and can thus be separated from the band 0 population, which map to $p = \hbar q$ under time-of-flight. Plotting the relative population in each band as a function of the modulation frequency gives a narrow resonance peak, as shown in figure 4.5.

4.5 Summary

Three different methods of lattice depth calibration has been investigated, and their practical use demonstrated. Each method has both advantages and disadvantages, however, and the choice between the three thus depends on several parameters.

Both the Landau-Zener tunneling method and the lattice modulation method gives data which can easily be interpreted. For the lattice modulation, the curve of potential depth versus resonant modulation frequency is sufficient to inter-

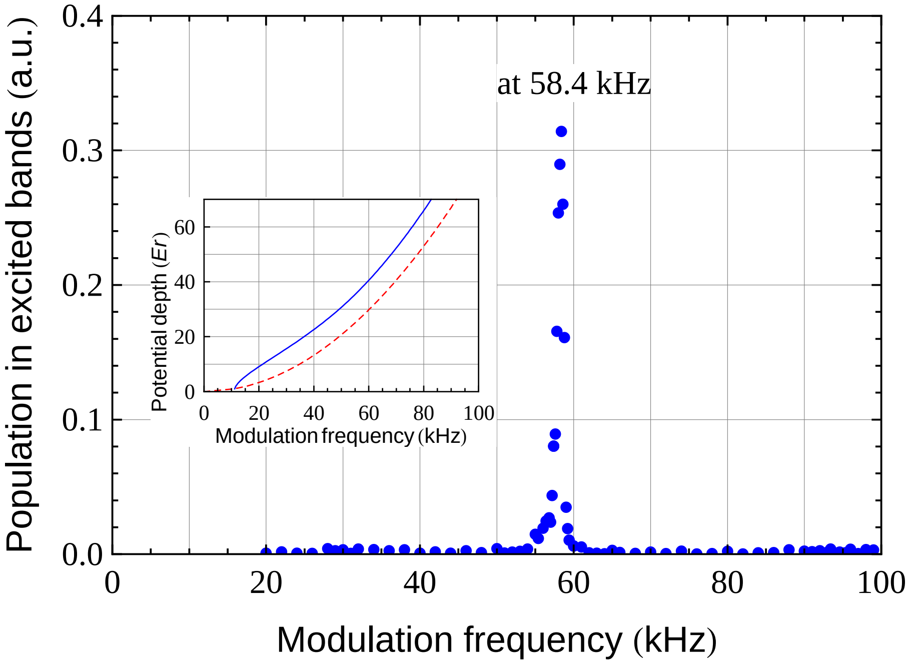

Figure 4.5: The atoms are excited by modulating the depth of the optical lattice, and the population in the excited band is measured by adiabatically mapping the atoms in each band to the free particle momentum space (see text). The narrow resonance at 58.4 kHz comes from the energy difference between band 0 and band 2, corresponding to a lattice potential with a depth of 38.7 E_r (blue solid curve in the inset). The insert displays the discrepancy between the harmonic oscillator level-splitting (red dashed curve in the inset) and the calculated distance at $q = 0$ between band 0 and 2 (blue curve in the inset)

pret the results. One should, however, be cautious that the implementation of lattice modulation used here assumes that the widths of both band 0 and 2 are negligible. The method is thus primarily useful for large lattice depths. Another complication is that it can take a long time to find the resonance to begin with, if no good initial guess exists.

Lattice calibration by Landau-Zener tunneling also gives a fairly simple analysis of the experimental data. The critical acceleration a_c can be extracted from the observed splitting ratio r and the known acceleration a, and compared with tabulated values from a 1D band-structure calculation. When using only the gravitational acceleration, however, it covers just a narrow range of lattice depths. This limits its practical usefulness in our current setup.

The Kapitza-Dirac method, with a 1D bandstructure calculation being called repeatedly in the loop of a numerical fitting algorithm, is more involved in terms of data-analysis than the other methods. Once implemented in the lab routines, however, a clear advantage is that it applies to a much broader range of lattice depths, and is experimentally straight forward.

Chapter 5

Dynamically Controlled Lattices

The main results of this chapter are to be published in [36].

5.1 Introduction

This chapter reports on the splitting of a BEC in the presence of a time-dependent optical lattice potential. First we demonstrate that a matter wave packet can be divided into a set of discrete momentum components, whose number and fractions can be precisely controlled using a time-dependent lattice depth. Next we study an atomic Bose-Einstein condensate, which is set in motion by displacing the magnetic trap, in the presence of time-dependent optical Bragg mirrors. We demonstrate high-order Bragg reflection of the oscillating condensate due to multi-photon Raman transitions, and we demonstrate the initial steps toward realizing a recombination of a split condensate in a harmonic trap.

5.2 Overview

Two distinct scenarios are investigated. In a first experiment we initiate Bloch oscillations in a vertical lattice under the constant force of gravity. Time-dependent control of the Landau-Zener tunneling rate enables us to realize a controlled matter wave beam splitter and a coherent matter wave source with controlled output coupler.

In a second experiment we investigate the coherent splitting of a Bose-Einstein condensate with an optical lattice in the presence of an external magnetic trapping potential. This allows us to investigate a matter wave splitter based on high-order Bragg reflection. Finally, time dependent first order Bragg-mirrors in a harmonic trap demonstrate multiple splittings of a condensate.

The dynamics of a condensate in an optical lattice is governed by the band structure of the periodic potential. The quadratic energy spectrum of a free particle splits up into bands which are labeled by the eigenenergies $E_n(q)$ with the eigenstates $|n, q\rangle$, where n denotes the band index and q the atomic quasimomentum, as described in chapter 3. The bands are separated by energy gaps whose size depends on the lattice depth as shown in Fig. 5.3. As a consequence the dynamics of an atom moving in such a potential is dramatically altered.

If an atom is subject to a force along the lattice axis, the band structure causes the atom to start oscillating instead of being constantly accelerated. These so-called Bloch oscillations occur, since an atom is Bragg reflected as it approaches the edge of the Brillouin zone. The Bloch period is given by $\tau_B = 2\hbar k_r/(ma)$, where $k_r = 2\pi/\lambda_{\mathrm{Lat}}$, m is the atomic mass, and a is the acceleration. The Bloch period corresponds to the time it takes for the atoms to be accelerated from one end of the Brillouin zone to the other. If the lattice beams are arranged to create a periodic potential along the vertical direction, a condensate can be held against gravity for several seconds in a sufficiently deep lattice potential, while the atoms perform Bloch oscillations.

When the lattice potential is reduced and the band gap narrows, Landau-Zener tunneling between Bloch bands starts to occur. In this regime the tunneling probability can be calculated from Landau-Zener theory. If the condensate is moving with acceleration a through the avoided crossing region of the $E_{n-1}(q)$ and $E_n(q)$ bands, the tunneling probability can be approximated by

$$P_t(n) = \exp\left(-\frac{a_c}{a}\right) = \exp\left(-\frac{\pi\Delta_n^2}{4nk_r a\hbar^2}\right) \tag{5.1}$$

[13] where we give the generalized expression for tunneling between bands n and $n-1$ for future reference. Here a_c is the critical acceleration, Δ_n is size of the band gap at the quasimomentum $n\hbar k_r$, and a is the acceleration of the atoms with respect to the lattice rest frame. In the experiments described in Sec. 5.3, the acceleration a is determined by gravity, while in Sec. 5.4 a is related to the slope of the harmonic potential at the instantaneous position of the atoms. The generalization to $n > 1$ follows from section 4.3.2 by noting that α in equation 4.4 is linear in n.

Since the experiments are carried out with ensembles of particles, their interaction modifies the single particle band structure outlined above. This effect is most pronounced at the edge of the Brillouin zone and can be described by a mean-field nonlinearity that causes a modification of the tunneling behavior. The tunneling rates in two directions between the Bloch bands also become different [24]. This work, however, is restricted to the weak interaction regime, where the tunneling probability is well approximated by the Landau-Zener formula. Experimentally the tunneling probability is set by controlling the optical lattice depth and can be suppressed completely when the lattice depth is increased.

5.3 Controlled Matter Wave Beam Splitter

In a first set of experiments we demonstrate that time-dependent control of the Landau-Zener tunneling rate enables us to realize a controlled matter wave beam splitter and output coupler.

To initiate the splitting mechanism, the magnetic trap is suddenly switched off and the atoms evolve in the combined lattice and gravitational potential. The atoms start to perform Bloch oscillations and each time they reach the edge of the Brillouin zone a fraction of the atoms can tunnel to a higher band. If the lattice depth is chosen such that atoms in higher bands with $n \geq 1$ are not bound, these atoms start to fall under the influence of gravity. Thus the condensate is split each time the edge of the Brillouin zone is encountered and atoms with $n \geq 1$ fall out of the lattice while Bragg reflected atoms remain trapped. If the tunneling probability $P_t(n)$ is held fixed and the initial atom number is N_0 the number of atom tunneling out of the lattice on the m'th Bloch period is $N_0(1 - P_t(1))^{m-1}P_t(1)$ and $N_0(1 - P_t(1))^m$ atoms remain in the lattice. This mechanism was indeed used within the first experiments with Bose-Einstein condensates in optical lattices [3] and later investigated in detail [30, 10, 24].

Alternatively however, the dynamical control available in experiments with optical lattices can be used to enhance this static situation. If the lattice depth is controlled synchronously with the Bloch oscillation period, the tunneling rate can be controlled individually for each tunneling event and thus the fraction of outcoupled atoms can be determined at will for each Bloch cycle.

Within our experiments the following sequence is used to realize this beam splitter. After production of a Bose-Einstein condensate the magnetic trap is switched off to release the atoms. Within this process the atoms receive a small initial upwards velocity of $9\,\mathrm{mm/s}$ and hence reach $q = 0$ after $920\,\mu\mathrm{s}$ due to gravity.

The Bloch oscillations are initiated by turning on the lattice at a depth suf-

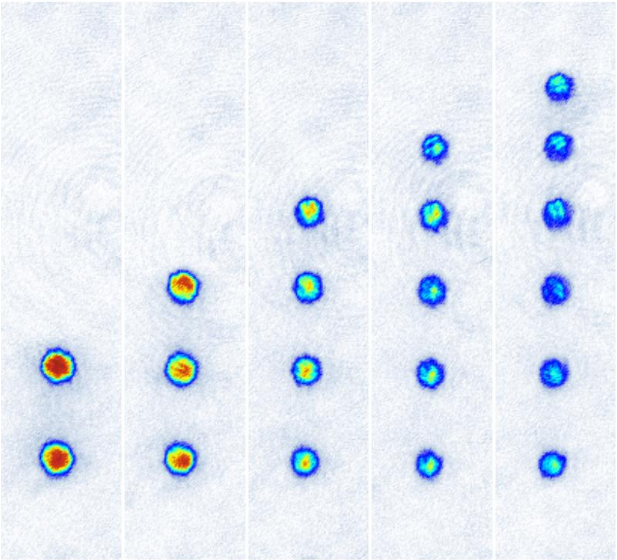

Figure 5.1: The condensate is divided n sub-condensates using time-dependent control of the tunneling probability. In order to produce n sub-condensates with the same fraction, the tunneling probability is controlled by adjusting the lattice depth for each Bloch cycle. For example, tunneling probabilities of 1/6, 1/5, 1/4, 1/3, 1/2 are used to produce 6 clouds with the same size as shown on the right.

ficient to completely suppress Landau-Zener tunneling (typically 2.4 E_r) after the atoms have started to move downwards, and before reaching the Bragg momentum ($\hbar k_r$). The lattice depth is ramped up within 200μs which is fast compared to the Bloch period $\tau_B = 1.0$ms, and sufficiently slow to ensure that the free space momentum is mapped to the zeroth band state with corresponding quasi momentum. To tailor the emission we then adjust the lattice depth for each subsequent Bloch oscillation to enable controlled Landau-Zener tunneling. The fraction of outcoupled atoms is given by Eq. 5.1.

Figure 5.1 shows that the condensate can thus be divided into n sub-condensates by varying the tunneling probability according to $1/n$, $1/(n-1)$, ..., $1/2$ for subsequent Bloch cycles and releasing the last one without splitting.

Time-dependent control of the optical lattice depth can also be used to completely suppress the tunneling by increasing the lattice depth. In Fig. 5.2 we illustrate such controlled splitting of matter waves by releasing three matter wave packets with the same size while blocking the tunneling for three Bloch periods.

The precise control of the emission of matter wave packets demonstrated here is available for several tens of Bloch oscillations, but the time scale of the

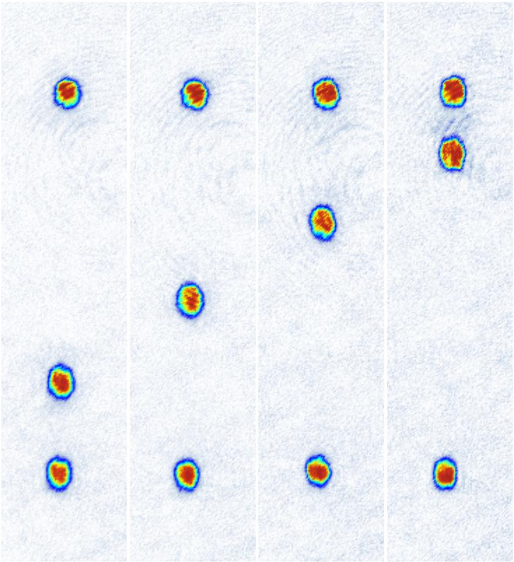

Figure 5.2: The condensate is divided into 3 sub-condensates which are released on selectable Bloch cycles. The first (bottom) and last (top) wavepackets are released in Bloch oscillation cycle 1 and 6. The third one between them is released during cycle 2, 3, 4 or 5, while tunneling is completely suppressed for the other Bloch cycles.

experiments is ultimately limited by the presence of interactions in the Bose-Einstein condensate, which destroy the Bloch oscillations. However, recently long-lived Bloch oscillations [17, 22] have been realized by using Feshbach resonances to strongly reduce the interaction strength. This technique could potentially also be used here to extend the number of available Bloch oscillations, and thus wave packets.

Moreover, the outcoupler presented here can also be employed if a set of wavepackets with different quasimomenta are present in an optical lattice. In that case, produced e.g. by phase-matched scattering [8, 23, 19], a set of matter waves oscillate in the lowest band with different phases, and each one could be emitted or retained selectively with the time-dependent outcoupler.

5.4 Matter Wave Splitting in Harmonic Trap

In a second experimental approach we investigate the coherent splitting of a Bose-Einstein condensate with an optical lattice in the presence of an external magnetic trapping potential. This approach allows us to investigate both a matter wave splitter based on high-order Bragg reflection and multiple splittings of a matter wave.

To induce motion, the minimum of the combined gravitational and magnetic potential is suddenly shifted in the y direction (the vertical axis) by increasing the current to the QUIC coils (from 150 A to 200 A). After this displacement, the BEC undergoes harmonic motion with an amplitude of 89.6 μm and oscillation period $T = 19.5$ ms. For future reference we define the first and second turning points at $t = T/2$ and $t = T$ as P1 and P2, respectively. In the experiment, we focus on the Bragg reflection and Landau-Zener tunneling of a BEC as it is accelerating and decelerating in the external potential. After triggering the harmonic motion in the magnetic trap, an optical lattice potential along the y-axis is briefly applied to the BEC at different times to induce the controlled splitting.

We have previously discussed the dynamics of a BEC initially at rest as it is being accelerated across the band edge. If, on the other hand, a condensate with high initial momentum is decelerated while in a lattice, Landau-Zener tunneling between higher excited bands and higher order Bragg reflection can happen depending on the lattice depth (see Fig. 5.3). In the harmonic external confinement this occurs as the condensate approaches one of the classical turning points coming from the trap center.

Bragg scattering for atoms can be described as a multi-photon Raman process, in which an atom of initial momentum $p = n\hbar k_r$ along the lattice axis is transferred to a superposition of the initial momentum state and the state with momentum $p = -n\hbar k_r$. The integer n is the order of the Bragg scattering, and obviously $2n$ photons are exchanged for each scattered atom.

Let us consider an atom moving from higher to lower bands. Remember that in the overall harmonic external confinement this means that in position space the atoms are approaching one of the turning points. As illustrated in Fig. 5.3, even the higher band-gaps open at sufficiently large lattice depths, which means that different orders of Bragg reflection can occur at the avoided crossings.

We denote the partially reflecting Bragg mirror at the transition from band n to band $n-1$ by BM$_n$. For example, for the potential depth of 4.6 E_r, Fig. 5.3 (middle) shows how part of the condensate is Bragg reflected on BM$_2$ in a 4-photon process. If the lattice is kept on, the transmitted (and thus still decelerating) fraction will subsequently reach BM$_1$, where it is fully reflected. In real space this corresponds to the second-order Bragg reflected part of the cloud reversing direction of propagation, whereas the unreflected part continues being decelerated until it is first-order Bragg reflected without reaching the classical turning point.

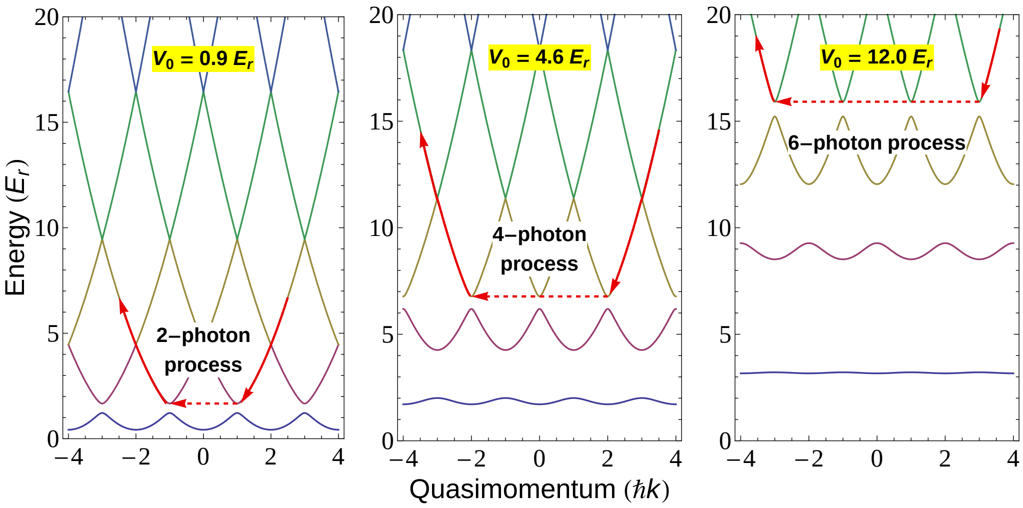

Figure 5.3: High-order Bragg reflection scheme. Half of the condensate is reflected on BM_1 (left), BM_2 (middle), or BM_3, which correspond to the first-, second-, and third-order Bragg reflection, respectively. When the fraction of the condensate transmitted through BM_n reaches the quasi-momentum corresponding to BM_{n-1}, it is fully reflected if the lattice is still turned on (see fig. 5.4 (b) and (d)). Otherwise only the single BM_n splitting occurs, resulting in $2n\hbar k$ momentum difference between the split components (fig. 5.4 (a), (c) and (e))

5.4.1 High Order Bragg Reflection

In the first experiment we apply the lattice before reaching the turning point (P1). Varying the time at which the lattice is ramped up, the motion in the external confinement allows us to implement an initial quasi-momentum in bands n=1,2, and 3. In each case we adjust the lattice depth to implement a tunneling probability of about $P_t(n) = 0.5$. Since the duration at which the lattice is pulsed on is short compared to the total oscillation period, T, we can consider the dynamics to occur at a single spatial point. This means that the force can be considered uniform throughout the duration of the lattice dynamics.

For the lowest lattice depth, Fig. 5.4 (a), the dynamics is simply a 50/50 splitting, followed by a short period of propagation in the lattice for both clouds. The release and subsequent time-of-flight ($t_{\mathrm{TOF}} = 12$ms) shows two clouds separated by approximately $x_{\mathrm{TOF}} = \frac{2\hbar k}{m} t_{\mathrm{TOF}}$, where m is the atomic mass.

For the deeper lattices, however, we first realize a 50/50 splitting on BM_n followed by a complete n-1'st order Bragg reflection on BM_{n-1} for the part that tunneled to a lower band. By turning off the lattice before the tunneled and

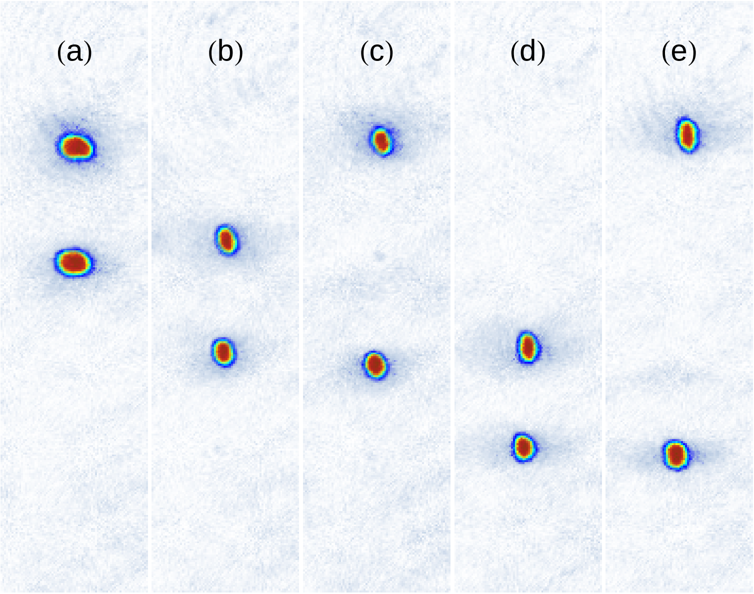

Figure 5.4: Time-of-flight images. The condensate is split by the interaction with optical lattices with the depth of (a) 1.1 E_r, (b) and (c) 5.0 E_r, (d) and (e) 13.5 E_r. The upper cloud in (a), (c), and (e) is the fraction without any reflection, and the lower cloud in all images is the one reflected from BM_n, i.e. BM_1 for (a), BM_2 for (b) and (c), BM_3 for (d) and (e). The upper clouds of (b) and (d) have been transmitted on BM_n and subsequently reflected on BM_{n-1}.

reflected part comes back to the BM_n mirror, we expect two peaks separated by x_{TOF} but shifted by $(n-1)x_{\mathrm{TOF}}$ relative to the BM_1 case. This can be seen in Fig. 5.4 (b) and (d).

The second, full Bragg reflection can be avoided by turning off the lattice before $q = (n-1)\hbar k$ is reached. In this case, as illustrated in Fig. 5.4 (c) and (e), we get a cloud unaffected by the lattice and one shifted by nx_{TOF}.

This series of matter wave splittings demonstrates a large momentum transfer beam splitter [9, 13]. Our experiments thus show that higher-order Bragg reflections can be manipulated by controlling the lattice depth and pulse timing.

5.4.2 Recombination of Split Clouds

An interesting application of the beam splitting process would be to utilize the harmonic confinement to recombine parts of the cloud that have been split earlier. We investigate this by pulsing on Bragg mirrors in the vicinity of both turning points (P1 and P2) in the harmonic trap (see Fig. 5.5).

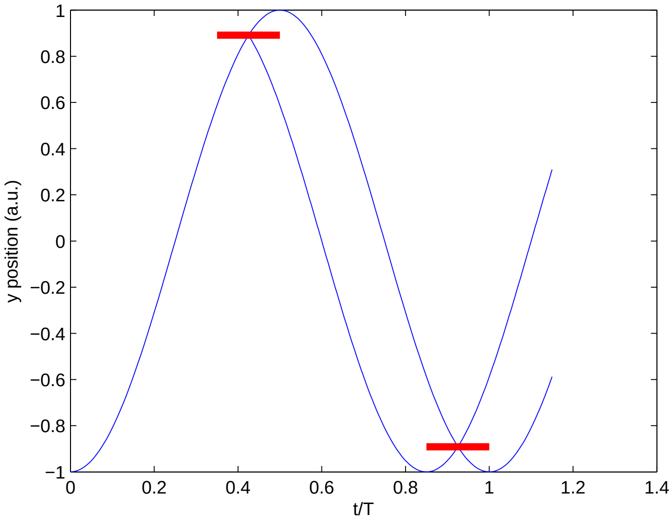

Figure 5.5: Principle of the recombination experiment. Blue curves show spatial harmonic oscillation of the condensate in the harmonic confinement, while the red lines schematically indicate the positions where the 50/50 BM_1 mirrors split the condensate. In the experiment of Fig. 5.6 (b), only the first Bragg mirror pulse is used, while in Fig. 5.6 (c), both are used.

Figure 5.6 (a) shows the condensate after the first two turning points (P1 and P2) without an optical lattice. A Bragg mirror (BM_1) with tunneling probability of 0.5 and duration less than one Bloch period is pulsed on briefly before the condensate reaches the turning point P1 to produce two equally split condensates with $2\hbar k_r$ initial momentum difference. The split wave-packets are reflected at the classical turning points P1 and P2, and then the images are grabbed after turning off the magnetic field and time-of-flight (Fig. 5.6 (b)). In addition to the intended vertical oscillatory motion, a significant difference in transverse position between the Bragg-reflected and transmitted clouds is evident. The origin of this transverse motion is currently being investigated.

In order to recombine the split clouds, we apply a 2nd Bragg pulse in the vicinity of the second turning point, P2, at the time when the two clouds are (ideally) spatially overlapped but with opposite momenta (see figure 5.5). The Bragg reflected part of the first cloud now has the same momentum as the transmitted part of the second and vice versa. Figure 5.6 (c) is the time-of-flight image taken when turning off the magnetic field 2 ms after passing the second turning point P2. As can be seen, unfortunately the transverse movement is so large that the recombined clouds are not spatially overlapped and therefore no

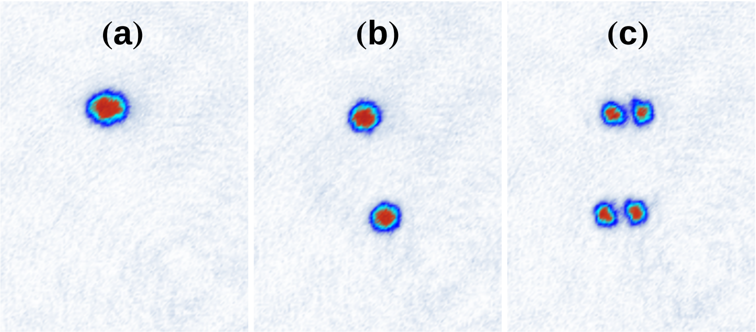

Figure 5.6: Images (a), (b), and (c) are taken at $t = 48$ ms, and trap is turned off at 21.5 ms, i.e. right after the second turning point, where momentum difference is large (see Fig. 5.5). (a) The BEC undergoes harmonic motion in magnetic trap potential without lattice light. (b) The BEC is split into two clouds by the Bragg mirror (BM_1) at P1. The two clouds are not on a vertical line (y axis) due to undesired motion along the z direction. (c) The split clouds are split again from the Bragg mirror (BM_1) at P2.

interference effects can be observed.

5.5 Summary

In summary, we have demonstrated high contrast coherent matter wave packet splitting using time-dependent control of the intensity of standing light waves. In this way the tunneling probability in each Bloch oscillation period was adjusted to control the outcoupled fraction dynamically, and even suppress tunneling completely.

We have furthermore demonstrated the dynamics of a BEC in a combined potential consisting of a magnetic trap and an optical lattice. We initiated BEC motion by suddenly displacing the magnetic trap, and used this to demonstrate high-order Bragg reflection. Finally, we have used two distinct Bragg-mirror pulses close to the classical turning points in a harmonic trap to (almost) implement a matter-wave Mach-Zender interferometer, which unfortunately so far is misaligned due to transverse motion in the trap.

Chapter 6

Quasi-Continuum Wavepacket Coupling to Localized States

The main results of this chapter are to be published in [27].

6.1 Introduction

In the preceding chapters dealing with single-particle bandstructure dynamics like Kapitza-Dirac scattering, Bloch-oscillation and Landau-Zener tunneling, the primary experimental detection technique has been time-of-flight imaging. Some of the described mechanisms, e.g. Bloch-oscillation, also display characteristic behavior in position-space, which could be probed directly. It might thus seem obvious to also image the condensate dynamics in direct space, rather than to map the reciprocal space using time-of-flight.

However, it is not obvious that such an approach could also provide useful results for condensates held in a combined lattice and magnetic trap. The tight magnetic confinement normally used during the evaporative cooling yields condensates that are barely resolvable with our imaging setup. And since the absorption-imaging beams are close to resonance, both the extraordinarily high in-trap optical density of the condensates, and the Zeeman-shifts due to the trap B-field, would seem to be prohibitively complicating factors, making time-of-flight imaging a better option.

By using weak magnetic confinement together with a 1D optical lattice with the option of amplitude modulation, in-trap imaging of condensates was, however, found experimentally to give very intriguing results. Both localized stationary states [34] and states displaying moving wave-packet characteristics was observed in-trap. This chapter presents some of the recent data and results that have so far come out of the investigation.

6.2 Experimental Setup

Following the evaporative cooling and BEC creation, the QUIC trap is relaxed to 12.3 and 37.9 Hz trapping frequencies in the axial and radial directions, respectively.

An optical lattice with a depth of typically $16\,\mathrm{E_r}$ is adiabatically turned on to load the BEC into the (mean-field) groundstate of the combined QUIC and lattice potential. The lattice is intensity-modulated (5-20% peak-to-peak amplitude) with a frequency ν for a variable time-span, (0.5-10 ms). After a variable hold-time, absorption images are taken in-trap.

6.3 Stationary Localized Atoms

Using a 10 ms modulation pulse, the in-trap images display patterns of "outlying" atomic clouds of varying optical density (see Fig. 6.1 and 6.2).

By varying the hold-time between modulation and imaging, the outlying clouds are found to be stationary, and they survive a complete turn-off of the magnetic trapping potential (see Fig. 6.3). The QUIC turn-off removes the diffuse cloud of quasi-continuum atoms visible between the central BEC and the outlying clouds, but leaves the positions of the peaks unchanged.

Figure 6.4 shows how diagonalization of the 1D Schrödinger equation with our trap potential leads to both localized and various degrees of delocalized eigenstates, which can explain the observed stationary states [34]. Figure 6.4 also shows clear similarities with the band-structure of periodic lattices, with "bands" 0, 1 and 2 below, and bands ≥ 3 in the quasi-continuum.

The numerical diagonalization of the symmetric 1D potential leads to solutions which are ± 1 eigenstates of parity. A particular eigenstate thus typically has a component localized on both the left and right flanks of a particular band. Moving away from the bottom of the band, however, the $P = \pm 1$ eigenstates form perfectly degenerate pairs. Physically this means that even though an atom initially localized on one flank is described as a coherent superposition of two split eigenstates, it will, due to the degeneracy, not tunnel from one side to the other.

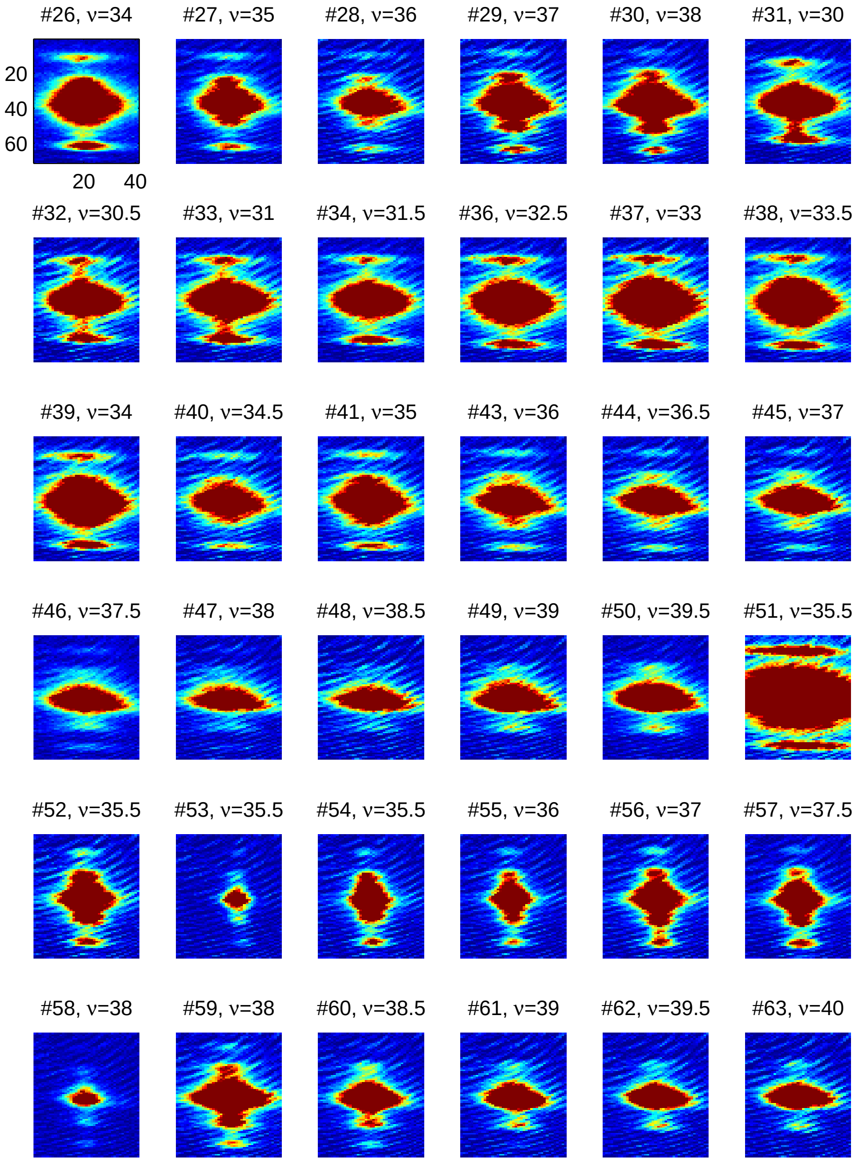

Figure 6.1: In-trap images of condensate and outlying peaks for different modulation frequencies. Image sizes are 40 × 70 pixels (square pixels, size $(1.94\,\mu\text{m})^2$).

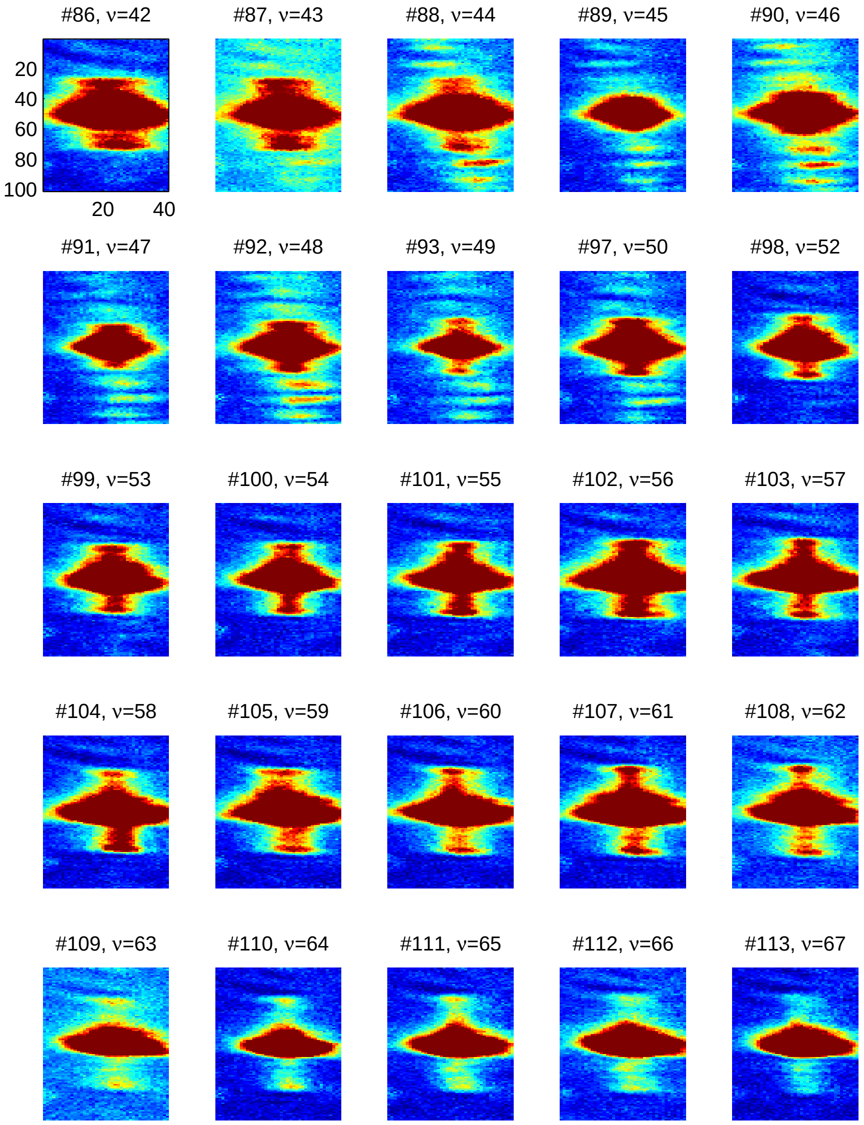

2010\week#43\2010−10−27\026_inSit

Figure 6.2: In-trap images of condensate and outlying peaks for different modulation frequencies. Image sizes are 40×100 pixels (square pixels, size $(1.94\,\mu\text{m})^2$).

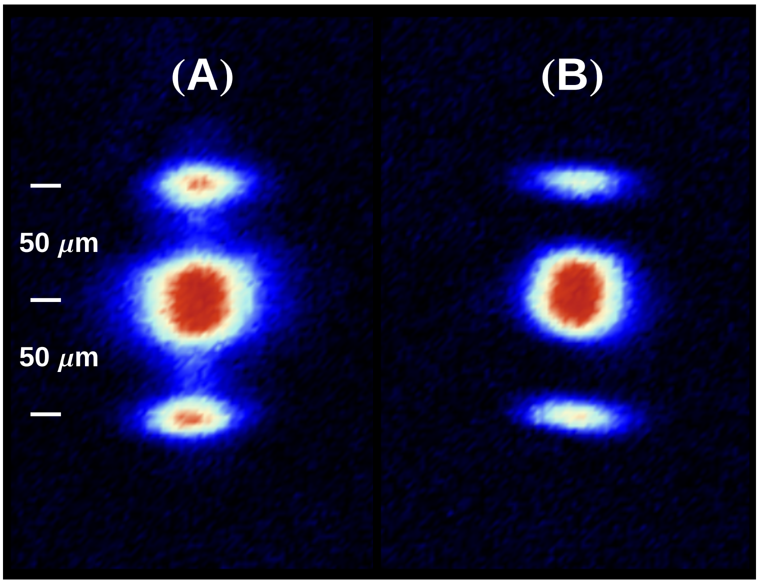

Figure 6.3: Outlying stationary clouds and central BEC imaged in superimposed vertical lattice and magnetic trap (A), and with the magnetic trap turned off during the hold-time (B). Both central BEC and outlying states are seen to be trapped by the lattice alone in (B).

6.4 Local Tilted Band-Structure Picture

Numerical diagonalization of the 1D Schrödinger equation into localized eigenstates gives an adequate description of the experimentally observed properties of the stationary states in the combined potential. The physical mechanisms involved can, however, be illuminated by a local tilted band-structure picture. This allows for an intuitive understanding of the transition between figure 6.3 (A) and (B), and connects nicely with the previous chapters. While less rigorous, this approach also helps in the interpretation of the non-stationary wave packets described below. Fundamentally, however, it is only a different perspective on the same physics.

The combination of the magnetic and lattice potentials is not periodic, since the harmonic confinement destroys the 1D periodicity of the lattice. The concepts of Bloch-oscillation and Landau-Zener tunneling can, however, still be applied here, due to the scale-difference between the relevant magnetic trap dynamics and the lattice spacing. A qualitative, if not quantitative, understanding of the experiments presented below can thus be gained by considering the harmonic confinement of the magnetic trap to be a "locally linear tilt" of the lattice. Wave-packets of narrow quasi-momentum distribution are thus ac-

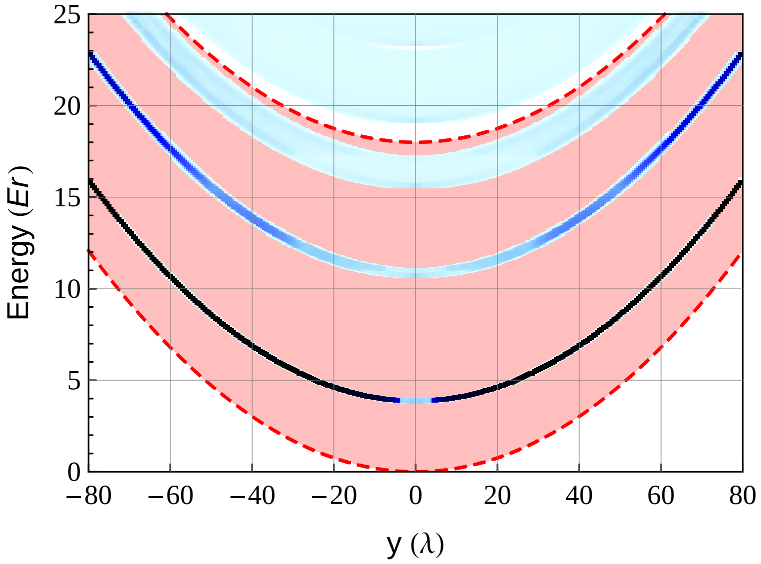

Figure 6.4: Spectrum of the 1D Schrödinger equation with combined cosine lattice potential $V_L = s\cos(kx)^2$, $s = 18E_r$, and harmonic confinement $V_B = \frac{1}{2}m\omega_0^2 x^2$, $\omega_0 = 2\pi \cdot 38.4\,\mathrm{Hz}$. The lower and upper dotted red lines (and shading in between) indicates V_B and $V_B + s$, while the black to light blue shading of the eigenstate solutions discriminates between localized eigenstates (black) to increasingly delocalized eigenstates (light blue).

celerated and undergo Bloch-oscillation or Landau-Zener tunneling under the assumption of constant acceleration. To use this picture, the quasi-momentum distribution cannot be infinitely narrow, however, since the spatial extent of the wavepacket must also be small compared to the motion in the harmonic confinement. It is thus a qualitative picture, which should be used with some care.

Considering the situation in Fig. 6.3 (B) in detail, we see that all 3 peaks are supported against gravity by the lattice alone. There are at least two mechanism by which this can occur. One is that the lattice is so deep that site-to-site tunneling is suppressed on the experimental timescale. The lattice depth used for Fig. 6.3 is $18\,\mathrm{E_r}$ (in the trap center), which corresponds to a total width of the zeroth band of $\hbar\omega$, with $\omega = 2\pi \cdot 40\,\mathrm{Hz}$. Even in the zeroth band, dynamics would thus be visible, although quite slow.

The other mechanism is repeated Bragg-reflections on the lattice potential, i.e. Bloch oscillations. Writing the band-gap, Δ, of equation 5.1 in units of the recoil energy, the critical acceleration determining if Landau-Zener tunneling will occur is

$$a_c = \frac{\Delta}{E_r}\frac{h^2\pi^2}{8m^2\lambda^3} \tag{6.1}$$

i.e. $a_c = (\Delta/E_r) \cdot 34.3\,\mathrm{m/sec}^2$. With $\Delta/E_r \approx 7$ for the lowest band-gap and $\Delta/E_r \approx 4$ for the second, LZ-tunneling out of both 0th and 1st band is thus heavily suppressed, when considering the gravitational acceleration.

If we assume that Bloch-oscillation in some band is the mechanism supporting the atoms against gravity at all 3 positions, the Landau-Zener tunneling (and accompanying loss) out of the given band must be suppressed when the lattice is tilted due to gravity. And, consequently, the LZ-tunneling will be even more suppressed for any acceleration smaller than g.

Returning to Fig. 6.3 (A), we can estimate the local acceleration at the outlier-positions due to the harmonic confinement. With vertical trap frequency $\omega = 2\pi \cdot 37.9\,\mathrm{Hz}$, and offset distance $d = 50\,\mu\mathrm{m}$, the local acceleration $a = \omega^2 d$ is $2.8\,\mathrm{m/s}^2$, which is smaller than the gravitational acceleration. From the above considerations, the localized stationary states can thus be understood both in terms of localized eigenstates, and Bloch oscillation. Whether the Bragg-scattering is a first or higher order Raman-process will depend on the particular band in which the Bloch-cycle occurs, as described in chapter 5.

6.5 RF-Cut of Localized States

Here we consider the localized states arising with lattice depth $s = 16$ and modulation frequency $\nu = 32\,\mathrm{kHz}$. To confirm experimentally that no tunneling takes place between the observed stationary states while the magnetic trap is on, we can apply an "RF-knife", which works just like the standard RF forced evaporative cooling. Sweeping the RF frequency will flip the spin of any atoms passing through the resonance condition shell defined by $h\nu_{\mathrm{RF}} = \mu_B g_F |B(\mathbf{r})|$. The gravitational sag in the weak magnetic confinement is $x_{\mathrm{sag}} = g/\omega_0^2 = 173\,\mu\mathrm{m}$ ($\omega_0 = 2\pi \cdot 37.9\,\mathrm{Hz}$). It follows that a downward RF frequency sweep will flip the spins of the lower localized atoms first, then the central state, until finally reaching the upper localized state (since even the upper localized state is below the magnetic minimum in the trap). Figure 6.5 shows this process, while Fig. 6.6 shows that it is also possible to selectively remove the central component, while leaving the localized states untouched.

By removing all but the upper localized state, it is possible to do an isolated lifetime measurement on these atoms while both lattice and harmonic confinement is on. Figure 6.7 shows the result of cutting away all but the upper peak and waiting for a variable time after the end of the RF-sweep. The initial rapid

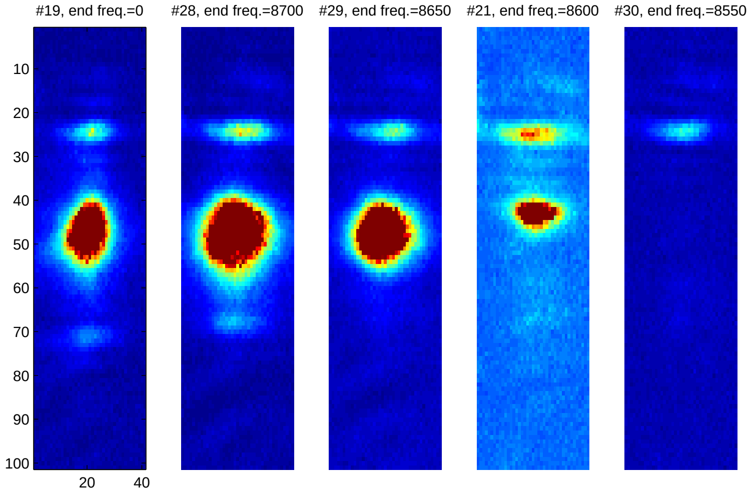

2010\week#44\2010−11−03\021_RF_sweep\

Figure 6.5: Cutting away lower and central in-trap peak with RF-knife.

decay was initially a surprise. With the approach of section 6.4, however, this is readily explained by noticing that an (accidentally) spin-flipped fraction of the upper state will still undergo Bloch-oscillation, and thus be confined in the vertical lattice direction, provided that the new local acceleration is not too large. The spin flipped atoms will thus not necessarily be expelled vertically due to gravity, but may leave the fitted region much slower by "spilling out" of the lattice beam sideways. In future RF-cut experiments, it is thus crucial to check this and, if needed, allow enough time for the atoms to escape before evaluating if the RF-cut is at the desired depth.

6.6 Band-Categorization of the Stationary States

Although the basic confining mechanism can be understood both from the localized eigenstates in Fig. 6.4 and from the suppression of LZ-tunneling in section 6.4, the above experiments have not addressed the question of which "bands" of Fig. 6.4 are actually involved.

To investigate this, we have mapped out the position of the localized peaks for a range of modulation frequencies ν. For the pictures in Fig. 6.1, the lattice depth is set to $s = 16$, the modulation duration is 10 ms, and the modulation frequency is varied. Each localized state is observed to move further away for increasing ν, and for frequencies in the range 36-39 kHz, two distinct localized peaks are visible on each side. Figure 6.8 shows the fitted distance between the

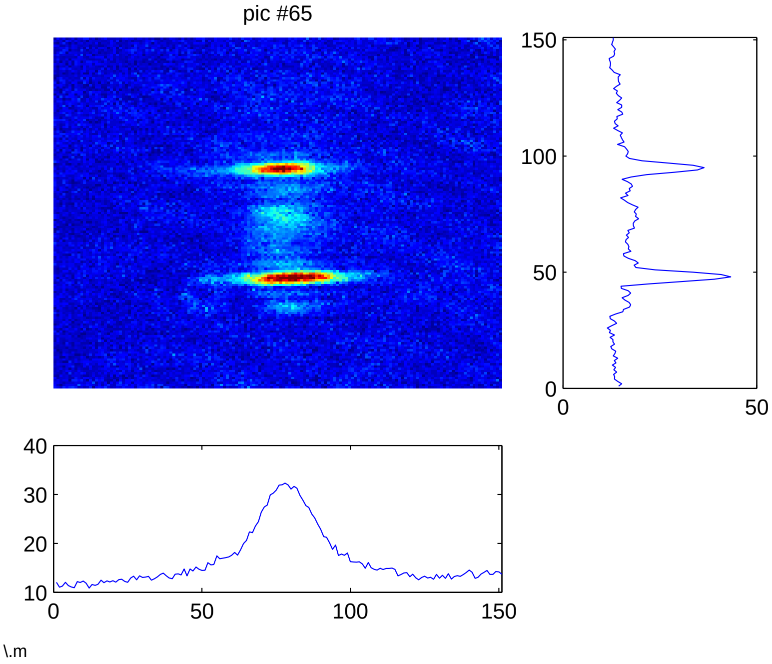

Figure 6.6: Cutting away the central peak with RF-knife. All dimensions in 1.94 μm pixels.

central peak and the peaks on the lower side.

The energy of an n'th band localized state with mean distance x to the trap center will have two distinct components, as can be seen from Fig. 6.4. One is the potential energy in the harmonic potential at x,

$$E_v = \frac{1}{2} m \omega_0^2 x^2 \tag{6.2}$$

while the other is the mean value of the n'th band-energy, averaged over the quasimomentum. Choosing $E_0(q = 0)$ as the energy reference (it is the initial state), the 1D bandstructure calculation of chapter 3 gives

$$\begin{aligned} E_1 &= \langle E_1(q) \rangle \\ &= 18.7\,\mathrm{kHz} \cdot \mathrm{h} \\ E_2 &= \langle E_2(q) \rangle \\ &= 33.4\,\mathrm{kHz} \cdot \mathrm{h} \end{aligned} \tag{6.3}$$

for the chosen lattice depth of $16E_r$.

To find the expected positions of localized states, we make the assumption that the total energy gained by the localized atoms during the vibrational

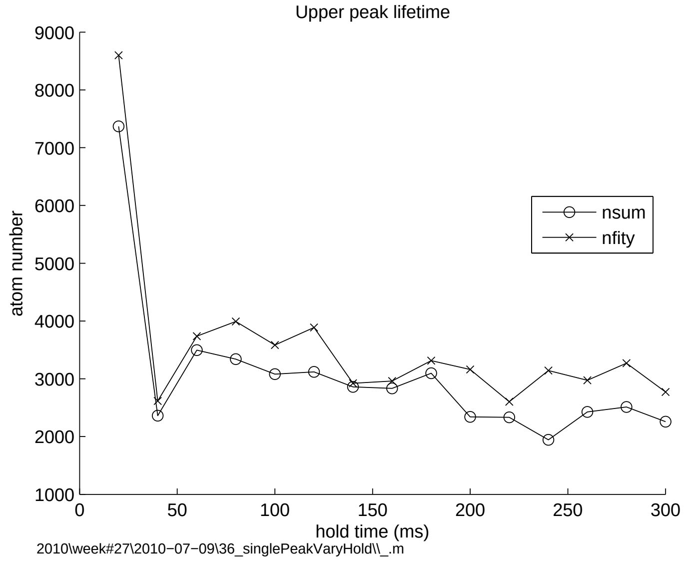

Figure 6.7: Lifetime measurement of the upper localized peak after cutting away lower and central states with RF-knife (two different atom number fit methods ploted). The initial decay is, most likely, the slow escape of spin flipped atoms in the upper peak (see text).

excitation is νh, such that

$$\nu h = \frac{1}{2} m \omega_0^2 x^2 + E_n \tag{6.4}$$

for a localized state in band n. This leads to the estimated mean distance from the trap center

$$x = 12.7\,\mu\mathrm{m} \cdot \sqrt{(\nu - E_n/h)/\mathrm{kHz}} \tag{6.5}$$

The square-root fits shown along with the points labeled n=1 data (upper curve) and n=2 data (middle curve) in Fig. 6.8 show very good agreement with the theoretical estimates from (6.5) and (6.3). We thus conclude that most of the observed peaks correspond to band 1 and 2 states, while no population has been detected in the localized band 0 states.

The third curve at the bottom may have an interpretation as classical turning-points for states in the third band. Since these are not localized states, the relevant parameter for this interpretation would instead be the energy $E_3(q = 0)$.

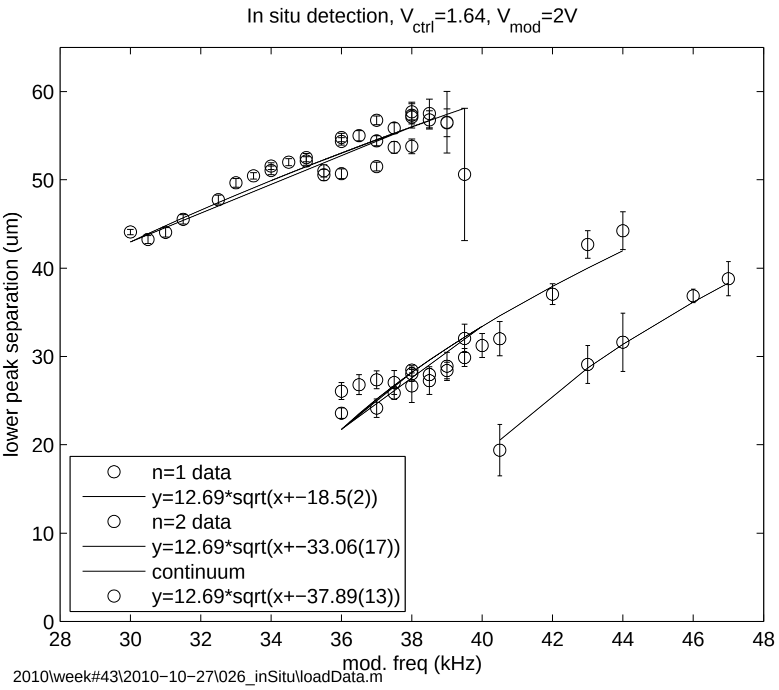

Figure 6.8: Fitted positions of the lower outlying peaks as function of lattice modulation frequency ν.

6.7 Quasi-Continuum Wavepacket Excitation

Having identified the stationary states as localized band 1 and 2 eigenstates, we need investigate the mechanism by which these states are being populated. Using a large amplitude, short ($500\,\mu\mathrm{s}$) lattice modulation at $\nu = 31\,\mathrm{kHz}$, a set of non-stationary "wave-packet" states is observed (see Fig. 6.9). Plotting the positions of the two wavepackets, shows how they move away from the center and turn around (Fig. 6.10).

To analyze this behavior in the local tilted bandstructure picture, consider the 1D bandstructure for the $s = 16$ lattice, shown in Fig. 6.11. A preliminary interpretation of the recently observed data is the following: During the $500\,\mu\mathrm{s}$ modulation pulse, a band 4 wave-packet centered around $q = 0$ (corresponding to extended quasi-momenta $\hbar q = \pm 4\hbar k_r$) is prepared in a two-step excitation. The transition is clearly off-resonant at the experimentally chosen frequency, but since the modulation is very strong, power-broadening ensures that the $|n = 4, q \approx 0\rangle$ state is populated.

The populated state is interpreted as two counter-propagating wavepackets, while the 8 photon Raman process, which is the physical origin of the band-

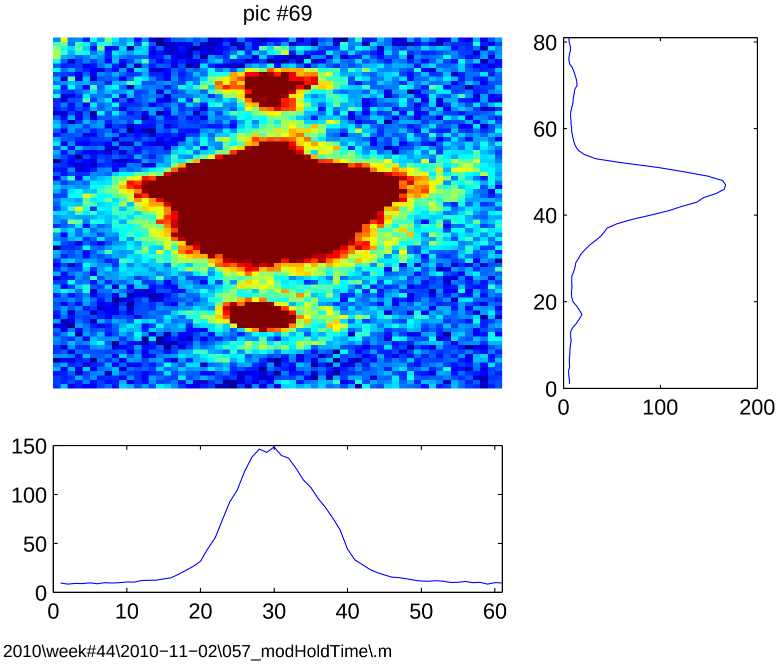

Figure 6.9: In-trap image showing the two moving "wavepackets". Image taken at 3 ms hold time after a 500 μs, $\nu = 31\,\mathrm{kHz}$ vibrational excitation pulse of large amplitude (2.16 V p-p, mean lattice depth set by 1.64 V signal on photo-detectors, corresponding to $s = 16$).

gap, is neglected. The corresponding "free particle" initial velocity of the wavepackets is thus

$$\begin{aligned} v &= \frac{4\hbar k_r}{m} \\ &= 20.1\,\mathrm{mm/s} \end{aligned} \tag{6.6}$$

Treating the quasi-momentum $\hbar q$ as the momentum of a classical particle moving in a harmonic trap (with $\omega_0 = 2\pi \cdot 37.9\,\mathrm{Hz}$), the times at which the quasi-momentum passes the avoided crossings at $q = nk_r$, $0 \leq n < 4$ are

$$t_n = \frac{\arccos\left(\frac{n}{4}\right)}{\omega_0} \tag{6.7}$$

giving $t_3 = 3.0\,\mathrm{ms}$. Subtracting the half the width of the $500\,\mu\mathrm{s}$ modulation pulse, the estimated time to observe a (6-photon Raman process) Bragg-reflection on the avoided crossing between band 3 and 2 in Fig. 6.10, would thus be at $2.785\,\mathrm{ms}$, and at a velocity of $15.1\,\mathrm{mm/sec}$. Both of these numbers agree very well with the data of Fig. 6.10, which cannot be explained by simple harmonic motion at ω_0.

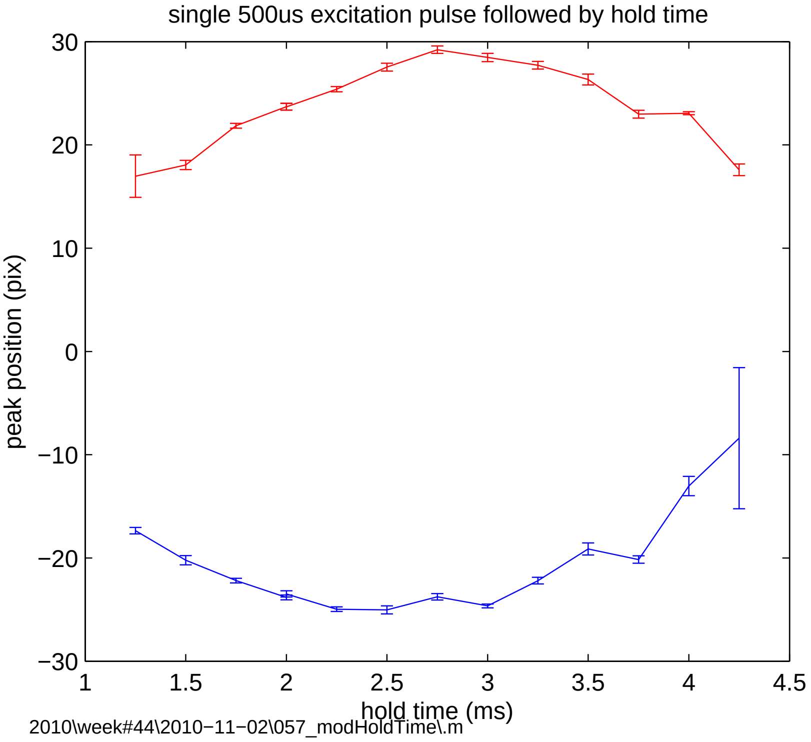

Figure 6.10: Fitted vertical positions of the two ”wavepackets” (see Fig. 6.9) as a function of hold-time. The turning-point is interpreted as a 6-photon Bragg scattering (see text).

6.8 Controlled Preparation of Localized States

The recent results of the preceding section suggests a cleaner way to populate the localized states, and opens up a wealth of interesting future experimental possibilities.

Firstly, the range of excitation frequencies that was observed to produce band 1 localized states in Fig. 6.8 was in the range 30 to 39 kHz. This roughly corresponds to the range of frequencies in the 2. band, and suggests that the band 2 states make it possible to populate higher-momentum states in a two step excitation.

To generate high momentum wave-packets without using excessive amplitude modulation, a possibility is thus to chose a lattice-depth, where the two steps are both resonant at $q = 0$. This occurs at approximately $s = 14$ with an excitation frequency of $27.6\,\mathrm{kHz}$ (for our λ of 914 nm), as shown in Fig. 6.12. This ensures that both of the two excitation steps will be resonant at $q = 0$.

However, instead of simply modulating the lattice at the corresponding fre-

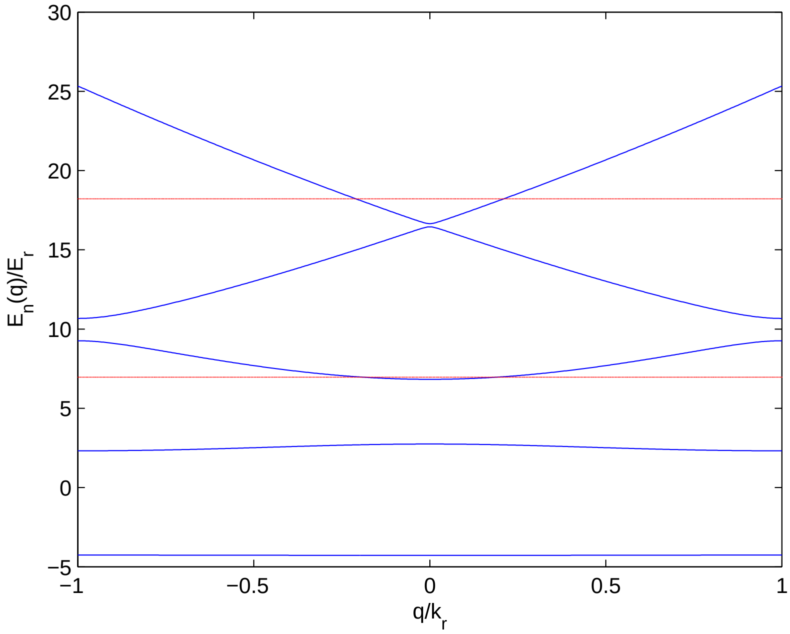

Figure 6.11: 1D bandstructure for $s = 16E_r$ lattice. Red lines indicate energies $h\nu$ and $2h\nu$ (relative to $E_0(q = 0)$) for the modulation frequency $\nu = 31\,\text{kHz}$.

quency, it may also prove interesting to use an adiabatic-following picture for the vibrational coupling. As is well known from e.g. optical and RF-transitions, the rotating wave approximation leads to time-independent coupling Hamiltonians, which have avoided crossings of the eigenstate levels at zero detuning. A degenerate two-step excitation thus corresponds to avoided crossings of three intersecting energy-levels. By sweeping the frequency, adiabatic following can thus be used to transfer the population from the lower to the upper state.

Returning to the localized states, the created high-momentum wave-packet now propagate away from the trap center and are decelerated by the confining potential. In the local band-structure picture, they thus loose energy. In reality, of course, this loss corresponds exactly to the potential energy gained in the harmonic confinement potential.

After moving down the band-structure curves of Fig. 6.11 or 6.12, a second lattice modulation pulse of identical or different frequency can now couple the third band to e.g. the first band, in which the wave-packet remains stationary due to Bloch-oscillations. Since this coupling occurs at a macroscopically different spatial position, the result is a localized trapped state, according to section 6.4.

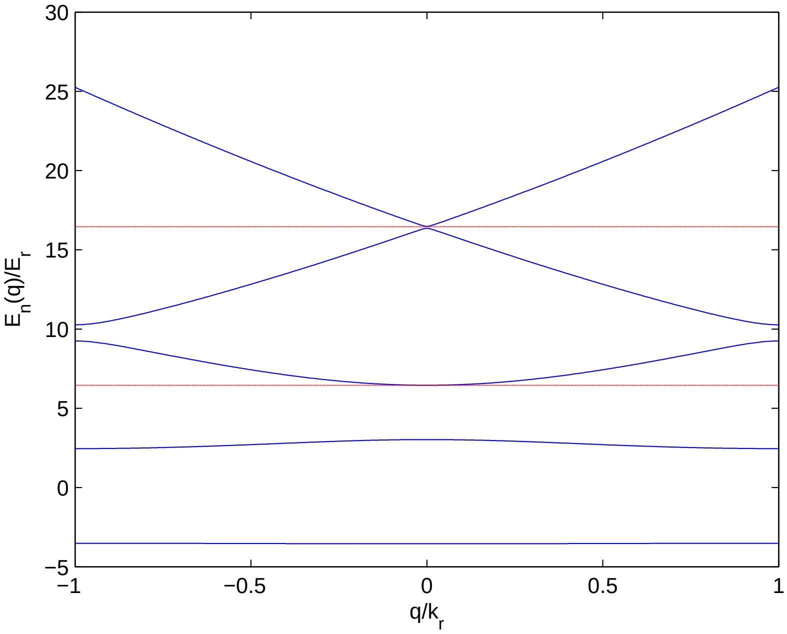

Figure 6.12: Two-step resonant excitation scheme for wavepackets. Red lines indicate energies $h\nu$ and $2h\nu$ (relative to $E_0(q=0)$) for 27.6 kHz.

While this scheme describes (in separated, discrete pump/probe steps), how the current 10 ms long excitation pulse could in principle populate the localized states, there are many other options. One could, for instance, ramp down the lattice intensity adiabatically as soon as the initial wavepackets are created, in order to avoid the Bragg-reflection seen in Fig. 6.10. In this way, the free-particle wave-packets would decelerate undisturbed down into the first or even zeroth band, after which the lattice intensity could be ramped adiabatically up again.

This scheme might seem elaborate, but the results from the previous chapters clearly show that dynamical adiabatic ramping of the lattice power on the Bloch-oscillation timescale τ_B is experimentally feasible. And for the wave-packet motion analyzed here, the accelerations are of the same order as g, or smaller, making it just as feasible in the current context.

Bibliography

[1] Analog Devices, One Technology Way, P.O. Box 9106, Norwood, MA 02062-9106, U.S.A. *400 MSPS 14-Bit, 1.8 V CMOS Direct Digital Synthesizer AD9954, Rev. 0*. [cited at p. 74, 75]

[2] Henrik Kjær Andersen. *Bose-Einstein condensates in optical lattices*. PhD thesis, Department of Physics and Astronomy University of Aarhus, Denmark, 2008. [cited at p. 9, 12, 15]

[3] B. P. Anderson and M. A. Kasevich. Macroscopic Quantum Interference from Atomic Tunnel Arrays. *Science*, 282(5394):1686–1689, 1998. [cited at p. 30, 41]

[4] M. H. Anderson, J. R. Ensher, M. R. Matthews, C. E. Wieman, and E. A. Cornell. Observation of bose-einstein condensation in a dilute atomic vapor. *Science*, 269(5221):pp. 198–201, 1995. [cited at p. 3]

[5] J. F. Bertelsen. *Ultracold Atomic Gases, Mixtures and Molecules*. PhD thesis, Department of Physics and Astronomy, University of Aarhus, 2007. [cited at p. 9, 15]

[6] Jesper Fevre Bertelsen, Henrik Kjaer Andersen, Sune Mai, and Michael Budde. Mixing of ultracold atomic clouds by merging of two magnetic traps. *Phys. Rev. A*, 75(1):013404, Jan 2007. [cited at p. 9]

[7] Immanuel Bloch. Exploring quantum matter with ultracold atoms in optical lattices. *Journal of Physics B: Atomic, Molecular and Optical Physics*, 38(9):S629, 2005. [cited at p. 27]

[8] Gretchen K. Campbell, Jongchul Mun, Micah Boyd, Erik W. Streed, Wolfgang Ketterle, and David E. Pritchard. Parametric amplification of scattered atom pairs. *Physical Review Letters*, 96(2):020406+, Jan 2006. [cited at p. 43]

[9] Pierre Cladé, Saïda G. Khélifa, François Nez, and François Biraben. Large momentum beam splitter using bloch oscillations. *Physical Review Letters*, 102(24):240402+, Jun 2009. [cited at p. 46]

[10] M. Cristiani, O. Morsch, J. H. Müller, D. Ciampini, and E. Arimondo. Experimental properties of bose-einstein condensates in one-dimensional optical lattices: Bloch oscillations, landau-zener tunneling, and mean-field effects. *Phys. Rev. A*, 65(6):063612, Jun 2002. [cited at p. 27, 30, 34, 41]

[11] Cypress Semiconductor, 3901 North First Street, San Jose, CA 95134. *EZ-USB FX2 Technical Reference Manual*, 2.1 edition. [cited at p. 79]

[12] K. B. Davis, M. O. Mewes, M. R. Andrews, N. J. van Druten, D. S. Durfee, D. M. Kurn, and W. Ketterle. Bose-einstein condensation in a gas of sodium atoms. *Phys. Rev. Lett.*, 75(22):3969–3973, Nov 1995. [cited at p. 3]

[13] J Hecker Denschlag, J E Simsarian, H Häffner, C McKenzie, A Browaeys, D Cho, K Helmerson, S L Rolston, and W D Phillips. A bose-einstein condensate in an optical lattice. *Journal of Physics B: Atomic, Molecular and Optical Physics*, 35(14):3095, 2002. [cited at p. 27, 28, 40, 46]

[14] Digilent, Inc., 215 E Main SuiteD — Pullman, WA 99163. *Digilent Parallel Interface Model Reference Manual*, 08/10/2004 edition. www.digilentinc.com. [cited at p. 79]

[15] Digilent, Inc., 215 E Main SuiteD — Pullman, WA 99163. *Digilent Port Communications, Programmers Reference Manual*, 06/03/05 edition. www.digilentinc.com. [cited at p. 79]

[16] Tilman Esslinger, Immanuel Bloch, and Theodor W. Hänsch. Bose-einstein condensation in a quadrupole-ioffe-configuration trap. *Physical Review A*, 58(4):R2664–R2667, Oct 1998. [cited at p. 13]

[17] M. Fattori, C. D'Errico, G. Roati, M. Zaccanti, M. Jona-Lasinio, M. Modugno, M. Inguscio, and G. Modugno. Atom interferometry with a weakly interacting bose-einstein condensate. *Phys. Rev. Lett.*, 100(8):080405, Feb 2008. [cited at p. 30, 43]

[18] Bryce Gadway, Daniel Pertot, René Reimann, Martin G. Cohen, and Dominik Schneble. Analysis of kapitza-dirac diffraction patterns beyond the raman-nath regime. *Opt. Express*, 17(21):19173–19180, 2009. [cited at p. 27]

[19] N. Gemelke, E. Sarajlic, Y. Bidel, S. Hong, and S. Chu. Parametric amplification of matter waves in periodically translated optical lattices. *Physical Review Letters*, 95(17):170404+, Oct 2005. [cited at p. 43]

[20] H. Goldstein. *Classical Mechanics*. Addison-Wesley, 1957. [cited at p. 4]

[21] Rudolf Grimm, Matthias Weidemller, and Yurii B. Ovchinnikov. Optical dipole traps for neutral atoms. volume 42 of *Advances In Atomic, Molecular, and Optical Physics*, pages 95 – 170. Academic Press, 2000. [cited at p. 18, 22]

[22] M. Gustavsson, E. Haller, M. J. Mark, J. G. Danzl, G. Rojas-Kopeinig, and H.-C. Nägerl. Control of interaction-induced dephasing of bloch oscillations. *Phys. Rev. Lett.*, 100(8):080404, Feb 2008. [cited at p. 30, 43]

[23] Karen M. Hilligsøe and Klaus Mølmer. Phase-matched four wave mixing and quantum beam splitting of matter waves in a periodic potential. *Physical Review A*, 71(4):041602+, Apr 2005. [cited at p. 43]

[24] M. Jona-Lasinio, O. Morsch, M. Cristiani, N. Malossi, J. H. Müller, E. Courtade, M. Anderlini, and E. Arimondo. Asymmetric landau-zener tunneling in a periodic potential. *Phys. Rev. Lett.*, 91(23):230406, Dec 2003. [cited at p. 41]

[25] H. J. Lewandowski, D. M. Harber, D. L. Whitaker, and E. A. Cornell. Simplified system for creating a bose-einstein condensate. *Journal of Low Temperature Physics*, 132:309–367, 2003. 10.1023/A:1024800600621. [cited at p. 9, 10, 13]

[26] K. B. MacAdam, A. Steinbach, and C. Wieman. A narrow-band tunable diode laser system with grating feedback, and a saturated absorption spectrometer for cs and rb. *American Journal of Physics*, 60(12):1098–1111, 1992. [cited at p. 10]

[27] S. Mai, S.J. Park, P. Winter, P. Pedersen, J. Sherson, and J. Arlt. Wavepacket dynamics and localized states in combined optical lattice and harmonic trap. *in preparation for Phys. Rev. Lett.*, 2010. [cited at p. 49]

[28] F. Mandl. *Statistical Physics*. Wiley, second edition, 1988. [cited at p. 5, 6]

[29] H. Metcalf and P. van der Straten. *Laser Cooling and Trapping*. Springer-Verlag, Berlin, 1999. [cited at p. 13]

[30] O. Morsch, J. H. Müller, M. Cristiani, D. Ciampini, and E. Arimondo. Bloch oscillations and mean-field effects of bose-einstein condensates in 1d optical lattices. *Phys. Rev. Lett.*, 87(14):140402, Sep 2001. [cited at p. 30, 41]

[31] Oliver Morsch and Markus Oberthaler. Dynamics of bose-einstein condensates in optical lattices. *Rev. Mod. Phys.*, 78(1):179–215, Feb 2006. [cited at p. 27, 31]

[32] Jongchul Mun, Patrick Medley, Gretchen K. Campbell, Luis G. Marcassa, David E. Pritchard, and Wolfgang Ketterle. Phase diagram for a bose-einstein condensate moving in an optical lattice. *Phys. Rev. Lett.*, 99(15):150604, Oct 2007. [cited at p. 28]

[33] OpenCores Organization, www.opencores.org. *WISHBONE System-on-Chip (SoC) Interconnection Architecture for Portable IP Cores, Rev. B.3*, September 2002. [cited at p. 77, 78]

[34] H. Ott, E. de Mirandes, F. Ferlaino, G. Roati, V. Türck, G. Modugno, and M. Inguscio. Radio frequency selective addressing of localized atoms in a periodic potential. *Phys. Rev. Lett.*, 93(12):120407, Sep 2004. [cited at p. 50]

[35] Yu. B. Ovchinnikov, J. H. Müller, M. R. Doery, E. J. D. Vredenbregt, K. Helmerson, S. L. Rolston, and W. D. Phillips. Diffraction of a released bose-einstein condensate by a pulsed standing light wave. *Phys. Rev. Lett.*, 83(2):284–287, Jul 1999. [cited at p. 28, 29]

[36] S.J. Park, S. Mai, J. Sherson, and J. Arlt. Dynamical control of quantum matter wave splitting using time-dependent optical lattices. *in preparation for Phys. Rev. A*, 2010. [cited at p. 39]

[37] S.J. Park, S. Mai, J. Sherson, and J. Arlt. Precision calibration of optical lattices. *in preparation for Appl. Phys. B*, 2010. [cited at p. 27]

[38] C. J. Pethick and H. Smith. *Bose-Einstein Condensation in Dilute Gases*. Cambridge University Press, 2002. [cited at p. 7, 22, 28]

[39] J. J. Sakurai. *Modern Quantum Mechanics*. Addison-Wesley, rev. edition, 1994. [cited at p. 4]

[40] T. A. Savard, K. M. O'Hara, and J. E. Thomas. Laser-noise-induced heating in far-off resonance optical traps. *Phys. Rev. A*, 56(2):R1095–R1098, Aug 1997. [cited at p. 20]

[41] I. B. Spielman, W. D. Phillips, and J. V. Porto. Mott-insulator transition in a two-dimensional atomic bose gas. *Phys. Rev. Lett.*, 98(8):080404, Feb 2007. [cited at p. 28]

[42] I. B. Spielman, W. D. Phillips, and J. V. Porto. Condensate fraction in a 2d bose gas measured across the mott-insulator transition. *Phys. Rev. Lett.*, 100(12):120402, Mar 2008. [cited at p. 28]

[43] Daniel A. Steck. Rubidium 87 d line data. Revision 1.6, 14 October 2003 available at http://www.steck.us/alkalidata. [cited at p. 20]

[44] K.-A. Suominen, E. Tiesinga, and P. S. Julienne. Nonadiabatic dynamics in evaporative cooling of trapped atoms by a radio-frequency field. *PHYSICAL REVIEW A*, 58(5):3983–3992, NOVEMBER 1998. [cited at p. 32]

[45] N. V. Vitanov and K. A. Suominen. Time-dependent control of ultra cold atoms in magnetic traps. *Phys. Rev. A*, 56(6), 1997. [cited at p. 32]

[46] D. Durfee W. Ketterle and D. Stamper-Kurn. Making, probing and understanding bose-einstein condensates. In *Proceedings of the International School of Physics-Enrico Fermi, IOS Press*, 1999. [cited at p. 14, 15]

[47] Carl E. Wieman and Leo Hollberg. Using diode lasers for atomic physics. *Review of Scientific Instruments*, 62(1):1–20, 1991. [cited at p. 10]

[48] Curt Wittig. The landau-zener formula. *J. Phys. Chem. B*, 109:8428–8430, 2005. [cited at p. 32]

[49] Xilinx. *Spartan-3 FPGA Family: Complete Data Sheet, DS099*, August 2005. [cited at p. 77]

Appendices

Appendix A

Configurable Digital Ramp Generator and DDS Programmer

A.1 Design Constraints

The purpose of the Configurable Digital Ramp Generator and DDS Programmer (from now on, the "FPGA-board") is to handle the serial programming of the DAC and DDS chips that provide analog control-ramps and swept frequency signals for multiple different purposes in the lab.

The DAC and DDS boards are placed in Euro-Rack modules around the lab. Previously these were programmed serially from one of the DIO 64 boards in the main computer, using long coax-cables. To have greater capacity, less cables filling up the lab, and less worries about impedance matching of cable terminations, the DIO 64 board driving the DACs will be replaced by multiple FPGA-board modules, each one placed in the same Euro-Rack as the DAC and DDS chips, it controls. A set of standard USB-2.0 hubs distributes data from the main (ECS) computer to the FPGA-boards.

A.1.1 Digital Ramp Generator

To lighten the computational burden on the main computer, the FPGA boards should handle the generation of linear ramps internally. I.e., to sweep the voltage of a particular analog channel from v_0 to v_1, the main computer should only need to send a short data package containing the essential parameters. Enumerating the ramp data packages for the channel by i, the parameters would be: start time $t_0(i)$, start value $v_0(i)$, end value $v_1(i)$ and slope of ramp $\alpha(i)$. The stop time $t_1(i)$ of ramp i is of course given implicitly by

$$t_1(i) = t_0(i) + \frac{v_1(i) - v_0(i)}{\alpha(i)} \tag{A.1}$$

If a second ramp $i+1$ has $t_0(i+1) > t_0(i)$, but $t_0(i+1) < t_1(i)$, the ramp generator should jump to the new ramp start value $v_0(i+1)$ at time $t_0(i+1)$ and continue on ramp $i+1$, without waiting to finish the ramp segment i currently in progress. Alternatively, if $t_0(i+1) > t_1(i)$, the output value of the generator should be kept constant on $v_1(i)$ in the time interval $t_1(i)$ to $t_0(i+1)$, where the new ramp i+1 would start from value $v_0(i+1)$. If ramp i is the last ramp segment, the value $v_1(i)$ should be kept until system reset or the start of a new experimental run. Aditionally, the ramp generator should handle the situation of $\alpha(i) = 0$ and/or $v_0(i) = v_1(i)$ gracefully.

The binary package format used to send the data actually uses $v_{low} = (\alpha > 0)\ ?\ v_0 : v_1$ and $v_{high} = (\alpha > 0)\ ?\ v_1 : v_0$ instead of v_0 and v_1, but this is just a technical detail chosen to make the implementation of the FPGA-logic slightly simpler.

The behaviour outlined above ensures that we can use the digital ramp generator seamlessly with the existing ECS system. We can still use non-linear ramps (S-curves, exponentials etc.) by using piecewise linear approximation, but the needed sample rate can be much lower than in the previous system, where every sample of the many channels were generated individually by the ECS computer.

A.1.2 DDS Programmer

Direct Digital Synthesis (DDS) constructs analog sine-waves with controllable frequency, phase and amplitude in the digital domain. We use the Analog Devices AD9954 DDS-chip for a few different purposes:

- To generate the RF frequency sweeps needed for the evaporative cooling.
- For the moving/accelerated lattice axis (z), two phase-locked AD9954 chips provide the AOM-controlled offset frequencies for the counter-propagating beams.
- Finally, an AD9954 chip is intended to provide an adjustable-frequency RF-input to a Mini-Circuits microwave-mixer for sideband generation.

The operation of the AD9954 is controlled by writing a set of internal registers through a serial port[1]. The settings do not take effect immediately, but only at the rising edge of the I/O update pin. One can thus load a new configuration into the internal registers and let the settings take effect at a latter time.

The AD9954 has several different modes of operation, and a few very counter-intuitive (and un-documented) surprises in store for the unwary. To cope with this, and to provide maximum flexibility, the DDS programmer module should not enforce a particular mode of operation. Instead, it should simply act as a "command sequencer". The i'th data-package written to the DDS programmer module should thus contain the following information: The time at which the settings should take effect $t_0(i)$, the number of bytes of data to write and the data-block itself. It is thus the responsibility of the calling application, not the DDS programmer, to ensure that the data-block conforms to the specifications of the AD9954. Only transfer of the data, and the timing of the subsequent I/O Update signal, is handled by the DDS programmer.

Refering to table 8 of the AD9954 manual[1], an example command block, setting the high and low frequency tuning words (FTWs) of a linear sweep to FTW0 = 0x11111111 and FTW1=0x2222FFFF, would be the 10 byte command: 0x0411111111062222FFFF. Here 0x04 and 0x06 are the addresses of the FTW0 and FTW1 registers. The linear sweep mode implemented internally in AD9954 is very similar to the operation of the ramp generator described above, including the behaviour when two ramps overlap in time. In a normal command, one would thus, in addition to FTW0 and FTW1, also set the registers determining the sweep rate.

The full details of the DDS programming modes is beyond the scope of this appendix. But it should be mentioned that the important linear-sweep mode of the AD9954 behaves somewhat unexpectedly if the FTW0/1 registers are reprogrammed while a sweep is in progress. A workaround is to formally always sweep the frequency upward from FTW0 to FTW1. Sweeps that physically go downward in frequency are then implemented using Nyquist frequency wraparound: The upper half of the possible values of the 32 bit FTWs corresponds to frequencies above the Nyquist frequency, i.e.:

$$f = f_s \times \tfrac{FTW}{2^{32}} \quad \text{for } 0 \leq FTW \leq 2^{31} \tag{A.2}$$

$$f = f_s \times \left(1 - \tfrac{FTW}{2^{32}}\right) \quad \text{for } 2^{31} < FTW \leq 2^{32} - 1 \tag{A.3}$$

where f_s is the externally supplied sample rate of the DDS, typically 400 MHz.

Because we do not have an absolute synchronization of the clock oscillators defining the frequency of the DDS chips and the timing of the FPGAs, we cannot avoid acquiring an arbitrary phase-shift if, at any point in a sequence of frequency sweeps, the sweep *direction* is changed. In all other cases (even for discontinuous frequency jumps), the phase will be continuous, unless explicitly programmed to have a discontinuous jump. Physically this means that if we want to investigate phenomena where the phase development of the quantum-system is referenced to the RF-field source (e.g. Stückelberg oscillations) *and* need to reverse the sweep direction during the interaction, a different linear-sweep mode of operation should be used. In other cases the Nyquist wrap-around technique should suffice.

A.2 Implementation of Ramp Generator and DDS Programmer

A.2.1 VHDL and the FPGA design work-flow

Internally FPGAs consist of small blocks of digital logic, typically 4-bit Look-Up Tables (LUTs) that can implement any Boolean function of 4 inputs and one output. Since this is equivalent to a 16 bit RAM block with individual addressing of each bit, the boolean function implemented by a LUT depends on what 16 bits of data it stores. Connecting together a large number of LUTs (and other, more specialized sub-circuits and RAM-blocks), one can implement very powerful digital processing in an FPGA.

Working directly with LUTs is not practical, just as few software programmers use assembly-code for large projects. Instead the design intent is captured in a higher-level "Hardware Description Language". The two most popular ones are called Verilog and VHDL, each having different strengths and weaknesses.

VHDL is the language used for the current project, and here, as with most languages, abstraction is the key to success. Abstraction and hiding of details is achieved through VHDL "entities". Semantically these correspond to the more well-known "classes" of object-oriented programming (OOP): Each entity can be instantiated many times (like objects). But while an OOP object consists of data with an associated set of imperative function routines, a VHDL "instance" becomes a real electronic sub-circuit constructed from LUTs, when the design is loaded into an FPGA. When its I/O-pins (called "ports" in VHDL lingo) are connected, an instance will thus respond to a given stimulus concurrently with the operation of all the other entity instances.

Larger projects are built as a hierarchy of entities, with each one containing instances of other (sub-)entities. These are then connected to each other and the ports of the enclosing entity through the VHDL-equivalent of electric wires, called "signals".

A finished VHDL design thus consist of an instance of the "top-level" entity, depending on many sub-entities. The ports of this top-level entity is mapped to (a subset of) the physical pins of the FPGA-chip using a "constraints file". An absolutely minimal design example having only a clock-signal input would thus map the physical clock-input pin of the FPGA to the clock-input port of the top-level VHDL entity.

Finally, the design is "synthesized" and "implemented" by software tools supplied by the FPGA vendor. This translates the VHDL description of the design to an explicit representation in terms of LUTs and their interconnections. Our FPGA boards have a Xilinx Spartan-3, XC3S1000 FPGA[49], and the integrated development environment used is the ISE Webpack from Xilinx.

To move the design into hardware, a binary configuration file is generated and loaded into the FPGA. Finally, when obvious design-bugs have been cleared out, the configuration file can be saved to a flash-ROM included on the FPGA-board, and a jumper set so that it will automatically be loaded into the FPGA at power-on. This is the operating mode that will be used in the laboratory.

A.2.2 Internal Bus Interconnect and USB I/O

To avoid unforeseen pitfalls, the top-level design of the VHDL code has been structured to conform with the well-tested "Wishbone" bus interconnection standard[33]. Several topologies are possible within this framework, but we use a shared bus topology similar to the one shown in figure A.1.

The `MASTER #i` and `SLAVE #j` modules shown are instances of VHDL entities that conform to the Wishbone standard. A `MASTER` modules can initiate a data transfer on the bus by setting its `CYC_O` output high. If no other `MASTER` modules are transferring data, the `ARBITER` module will then immediately grant ownership of the bus to the `MASTER` module by setting the appropriate `GNT()` and `GNT#` signals. If another `MASTER` is currently transferring data, the requesting `MASTER` is forced to wait for the current transfer to finish (because it won't receive an `ACK_I` signal from a `SLAVE`). And if two `MASTER` modules request ownership on the same clock cycle, the `ARBITER` will resolve the conflict using a round-robbin scheme.

Assuming that no conflicts occur, the data transfer will proceed according to the Write Enable signal, `WE_O`, of the active master module. If high, a data word is transfered from the master to a slave, otherwise a word is read from a slave by the master. The `ADR()` signal vector encode both which `SLAVE` module and which register internally in the slave is involved.

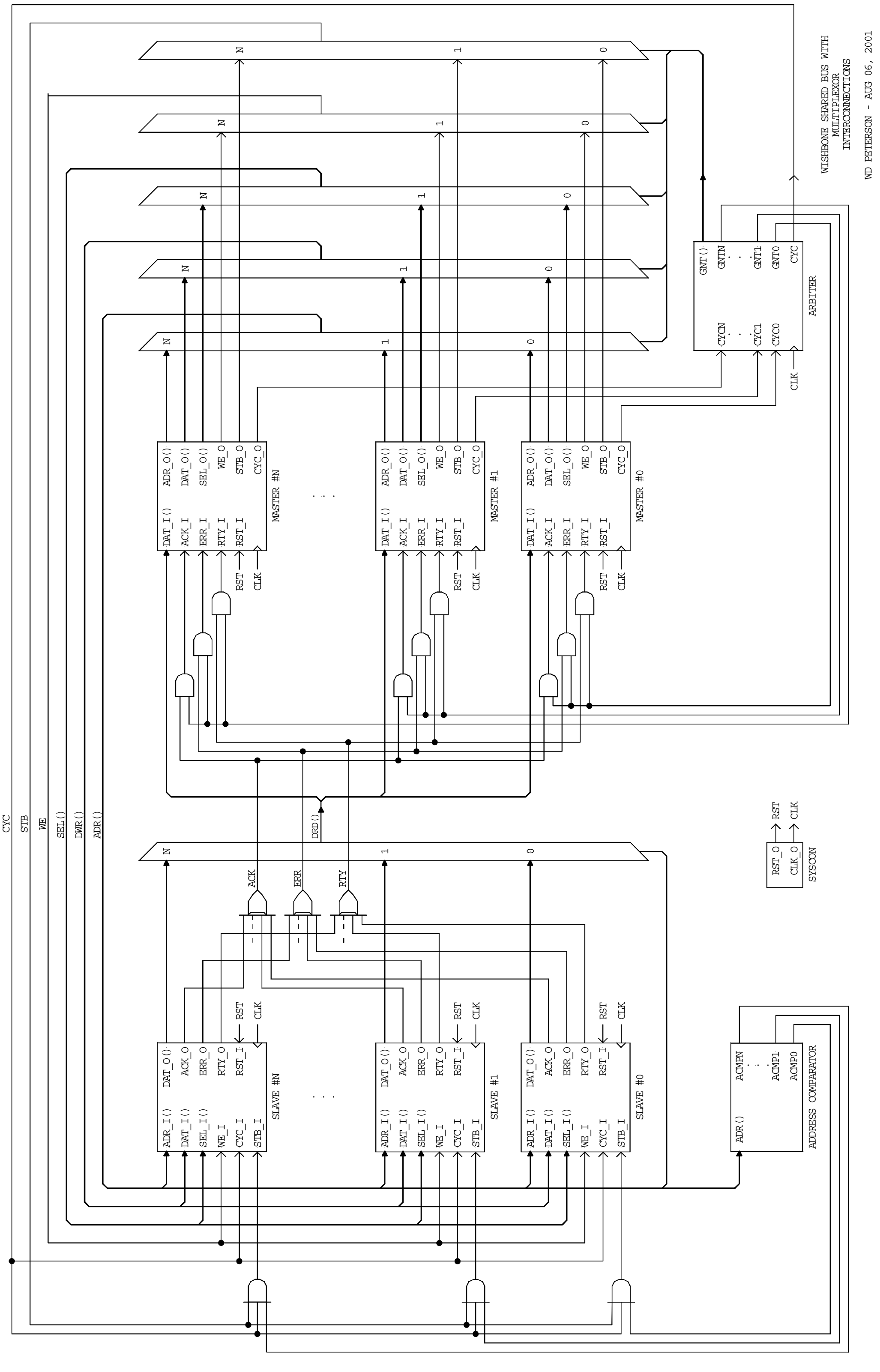

Figure A-22. WISHBONE shared bus with multiplexor interconnections.

WISHBONE SoC Architecture Specification, Revision B.3 130

Figure A.1: ”Wishbone” shared bus example. Figure from[33].

In the current project, the Wishbone interconnect (all the signals shown in figure A.1) has been dimensioned to accommodate up to 4 master modules and 32 slave modules. The with of both the address bus `ADR()` and data busses `DWR()` and `DRD()` is 8 bit. The most significant 5 bits of `ADR()` thus determines which of the 32 SLAVE modules gets a `STB_I` signal, while the least significant 3 bits determines which of the 8 possible internal registers of each SLAVE is addressed.

Many of the modules (entities) in the project can be classified as either Wishbone masters or slaves. To get an overview, the most important ones are:

Wishbone masters: The USB/EPP Communication module and the Data Redistribution Module.[*]

Wishbone slaves: Digital Ramp Generator, DDS Programmer, External Memory FIFO Module, System Control Module.

Non-Wishbone modules: DAC Driver Module.

A typical configuration instantiates one USB/EPP Communication module, one Data Redistribution Module, one System Control Module and one External Memory FIFO Module. The number of instantiated Digital Ramp Generator modules correspond to the number of analog channels driven by the FPGA-board, which is typically 16, 20 or 24. Corresponding to these numbers, there are resources left to instantiate 2, 1 or 0 DDS Programmer modules on each FPGA-board. The operation of these modules are described in turn below.

A.2.3 USB/EPP Communication Module

On the FPGA board there is, in addition to the FPGA itself, several other IC chips. One of them is a Cypress Semiconductor FX2[11]. This small CPU handles USB-2.0 data-traffic to and from the FPGA-board. The manufacturer of the FPGA-boards has programmed the FX2 with firmware that translates USB-2.0 data packages to/from the very simple EPP parallel port protocol[14]. Used together with an accompanying DLL module[15], it is thus quite simple to read/write single bytes on eight pins of the FX2 chip.

These eight bi-directional data-pins, along with a few handshake lines, are connected directly to pins of the FPGA. The purpose of the communication

---

[*] An experimental implementation of a 16 bit CPU core, that is not used in the final system, also belongs in the Wishbone masters category.

module is to connect this external USB/EPP communication interface to the internal Wishbone bus. By doing so, an application running on a computer connected via USB, is able to read and write to/from any address in any of the Wishbone slave modules instantiated in the FPGA.

A.2.4 Digital Ramp Generator

This module implements the requirements of the ramp generator outlined in section A.1.1. The detailed specification of the data-package format is as follows: t_0 (32 bit), v_{low} (16 bit), v_{high} (16 bit), sign of sweep direction s (1 bit) and unsigned sweep-rate r (31 bit).

The data-packages are written one byte at a time to the internal address 0 of the relevant ramp generator module. Internally this module has a 2048 byte FIFO-buffer with an 8 bit wide input port and 32 bit wide output port. Data written to address 0 is pushed onto this FIFO buffer.

At the other end of the FIFO a state machine compares the timestamp with a global 32 bit time signal. When there is a match, the rest of the data-package is read from the FIFO and into counters that produce the actual ramp output. This loading takes only few clock-cycles (at a clock-rate of $f_{clk} = 40$ MHz), so the state machine can handle very closely spaced ramp commands. They must be sorted according to timestamp, however.

The limiting values of the 16 bit output v is given by v_{low} and v_{high}, and the sweep-rate between these depend on r as follows:

$$\frac{dv}{dt} = \frac{s\, r\, f_{clk}}{2^{31}} \tag{A.4}$$

With the maximum value $r = (2^{31} - 1)$, v can thus sweep the full range of output, from $v = 0$ to $v = (2^{16} - 1)$, in 1.6 ms. Even though the sweep is internally in steps of 1, the sweep-rate is thus actually limited by the bandwidth of the analog circuitry buffering the DAC board outputs. At the other end of the scale, $r = 1$ corresponds to one LSB step of the output every 54 seconds, which should be more than adequate for any experiment.

A.2.5 DAC Driver Module

For every 4 Digital Ramp Generators, there is one DAC Driver Module. These generate the serial programming data for the connected DAC boards, with each board having 4 analog outputs.

The serial programming clock rate can be adjusted to avoid transmission errors in the cables connecting to the DAC boards. The 4×16 bit input signals are thus sampled at as high a rate, as the serial clock rate allows for. The lack of strict synchronization between the digital ramps and the serial output sampling is not expected to be a problem.

An advantage of the clean separation between the Digital Ramp Generators and the DAC Driver Modules is that, if the need should arise, it would be easy to insert a digitally configurable Proportional/Integral/Derivative (PID) feedback controller in between the two. The ramp generator would thus supply the target value, while the actual current value would be captured by a connected ADC. There are enough unused I/O-pins on the FPGA-boards to support a few external ADCs, but they have not been included in the standard design yet.

A.2.6 DDS Programmer

This module is very similar to the Digital Ramp Generator on the input side. Command packages are likewise stored into a 2048 byte FIFO buffer, and the data format is similar: t_0 (32 bit), number of bytes in the data-block, N, (8 bit) and data-block ($N \times 8$ bit).

The data in a block is sent serially to the connected DDS as soon as it becomes available in the FIFO. The state machine then waits for a match between t_0 and the global time. When this happens, the I/O Update pin on the DDS-chip is pulsed, after which the state-machine starts to load the next data-block, as it becomes available.

A.2.7 External Memory FIFO Module

A limitation in the above scheme is the limited depth of the 2048 byte FIFO buffers used in both the Digital Ramp Generators and the DDS Programmers. These FIFOs can only hold 170 of the 12 byte data-packages used in the ramp generator, and even less DDS commands. For long, linear sweeps, this is fully adequate. But using exponential or s-curve sweeps, one might need much more linear segments.

To accommodate the extra data on the FPGA-board, an on-board 16 MB RAM chip is used. The external memory FIFO module exposes 8 MB of this memory space as a FIFO buffer with 8 bit read and write port width.

The module is a Wishbone slave, and writing to its internal address 0 pushes data onto the FIFO buffer, while reading from 0 pops data off the FIFO. Notice here, that the Wishbone standard does not imply that reading from an address should return the data last written. An address can just as well represent each end of a large FIFO.

In the standard implementation, the external memory module is assigned the 5-bit Wishbone slave address 0. Reading and writing to the external FIFO thus both happens at the absolute address 0.

A.2.8 Data Redistribution Module

This module works in conjunction with the previous one as follows: Instead of writing the Digital Ramp data-packages and DDS command packages directly to their destination modules, all the commands are prepended with a header specifying the destination address (8 bit) and the amount of data in the command (8 bit). The commands are then sorted according to their time-stamp and written to the external FIFO buffer located at the absolute address 0.

The redistribution module, which is a Wishbone master, continuously monitors whether the external FIFO is empty. And when it is not, its state machine reads data from the FIFO and distributes it according to the address and data-size fields of the headers.

The module also monitors the "full" signal from the FIFO-buffers in all the receiving Ramp Generator and DDS Programmer modules, halting its operation as needed. The complex interplay of having two simultaneously active Wishbone masters (the communication and data redistribution modules) is handled gracefully by the Arbiter module.

A.2.9 Timing, Triggering and the System Control Module

Not all the functionality of this module has been implemented yet, but most of its intended functionality is already present in the top-level module, and collecting it into its own sub-entity is thus mostly a matter of making the code more tidy and readable. Its purpose is to control the overall operation and global control signals of the FPGA-board.

Presently, all important modules in the system are connected to a global RESET signal, which ensures a well defined starting condition for each sub-system (e.g. by clearing the many FIFO buffers and resetting state-machines). The RESET signal is connected to a push-button on the board and is also automatically asserted for a few clock-cycles after power-on. The System Control Module should, being a Wishbone slave, provide a set of registers that enable e.g. a global RESET to be initiated by software on the connected host-computer, and not only by manually pressing a button.

The timing and triggering is another important subject. Since the different FPGA-boards throughout the lab need to be in perfect synchronization, they use a common external time source. Presently the FPGA quadruples a 10 MHz laboratory reference clock using an internal PLL (Phase Locked Loop). The resulting 40 MHz clock is then used as the "logic clock" on each FPGA-board, to which everything else is synchronized.

When an external trigger-signal (connected on a dedicated BNC-input like the 10 MHz clock signal) is received, a 32 bit "current time" signal starts counting from 0 at a rate of 10 MHz. As described in the above sections, it is this "current time" signal that triggers the individual DAC and DDS ramps. Note however, that if DAC ramps or DDS commands with $t_0 = 0$ are written to the FPGA-board before triggering, they will execute immediately since the reset value of the time-counter is zero. This behavior is intended, as it supports setting startup-values on the analog channels and initial configurations of the DDS chips.

For added flexibility, future versions of the System Control Module should complement the hardware-triggered mode with a software trigger register, so that both experiments depending on a hardware trigger signal (e.g. the MOT fluorescence-level) and purely software triggered experiments can coexist in the same setup.